Initial Model Assessment for Intermediate-period Full-waveform Inversion of the Contiguous U.S and Surrounding Regions

---

submitted to *Geophys. J. Int.*

Initial model assessment for intermediate-period full-waveform inversion of the contiguous U.S. and surrounding regions

Tong Zhou [1⋆], Ziyi Xi [1], Min Chen [1,2] and Jiaqi Li [1]

[1] *Department of Computational Mathematics, Science and Engineering,*
Michigan State University, East Lansing, Michigan, 48824, *USA.*

[2] *Department of Earth and Environmental Sciences, Michigan State University,*
East Lansing, Michigan, 48824, *USA.*

SUMMARY

Since the completion of the EarthScope Transportable Array deployment across the contiguous U.S., there have been various 3-D seismic models with improved image resolution for the crust and upper mantle. However, discrepancies exist between these models due to the differences in both data sets and tomographic methods. It is an essential yet often missing step to evaluate these models and compare their predictability of seismic waveforms, which is helpful for guiding the interpretation and direction of further model refinement. In this work, we systematically evaluate eight 3-D seismic models by measuring the waveform similarity and misfit between observed data and synthetic data computed using these models. An independent validation data set consisting of waveforms from 30 earthquakes recorded by about 3,000 stations across the contiguous U.S., Canada and Mexico is used. The results show that existing 3-D seismic models well capture long-wavelength waveforms while have discrepancy in short-period body and surface waves, suggesting the smaller-scale structures and the radial anisotropy in the crust and upper mantle, especially in the sedimentary basins, are still less constrained. Our results suggest a hybrid model, with the crust constrained by both short-period surface waves (e.g., US.2016) and survey data (CRUST1.0), and with the mantle constrained by unbiased multiple data sets (e.g., S40RTS or S362ANI), can be used as a good initial model for further model improvement based on full waveform inversion.

Key words: model evaluation; waveform misfit; seismic tomography; computational seismology

1 INTRODUCTION

Seismic tomography provides one of the most important physical constraints of the Earth's interior structure and offers insight into the dynamic processes of the lithosphere and asthenosphere. Tomographic images of the Earth's interior, facilitated by large-aperture uniform array deployments (e.g., USArray in North America and CEArray in East Asia) have been tremendously improved in resolution of the crust and upper mantle structure (Yuan et al. 2014; Schmandt & Lin 2014; Chen et al. 2015b; Shen & Ritzwoller 2016; Zhu et al. 2017; Krischer et al. 2018; Tao et al. 2018). Meanwhile, advanced tomographic methods utilizing either multiple data sets (e.g., Shen & Ritzwoller (2016)) or full waveform inversion technique (e.g., Fichtner et al. (2009, 2010); Tape et al. (2010); Lekić & Romanowicz (2011); Yuan et al. (2014); Chen et al. (2015a, 2017, 2019); Zhu et al. (2017); Tao et al. (2018); Krischer et al. (2018)) have helped remarkably in accurately rendering the physical properties of the crust and mantle structure. Although large-scale structures (on the order of thousands of kilometers) in tomographic models of the same regions extracted from different datasets and/or tomographic methods are similarly captured in general, the small-scale structures (on the order of hundreds and/or tens of kilometers) are still very different in terms of both the amplitude and the pattern of seismic wave speed anomalies. These models also have different geometric mesh and seismic parametrizations (e.g., isotropic or radially anisotropic velocity), which brings extra complexity for interpretation and use of the tomographic models. From the inversion aspect, each model has achieved their best fitting on their own datasets using the corresponding forward simulation solvers. However, if examining the waveform fitting with a uniform and independent validation dataset,the waveform fitting for each model shows dis-

---

⋆

crepancies. These discrepancies become more severe when more realistic Earth's properties are taken into account, e.g., the topography, attenuation, and the Earth's ellipticity. Therefore, there is a need to further refine the seismic wave speeds model in contiguous U.S region within a full-waveform inversion framework that takes more realistic Earth properties and larger waveform datasets into consideration.

Full-waveform inversion methods usually adopt a gradient method (e.g., conjugate gradient) with the gradient calculated by the adjoint wavefield to update the model and minimize the misfit function such as the least-squares misfit of travel time, amplitude, waveform, or the zerolag cross-correlation coefficient (Tromp et al. 2005; Tao et al. 2017). However, these geophysical inversion problems are highly nonlinear which require a good initial model closer enough to the ground truth to prevent from being trapped into a local minimum when using the gradient-based methods (Mulder & Plessix 2008; Fichtner et al. 2009; Zhu et al. 2017; Krischer et al. 2018; Zhou et al. 2019). Therefore, it is important to select a good initial model for FWI. Over the years, the initial models for FWI works include a 1-D mantle model with 3-D crust (Lekić & Romanowicz 2011), a global 3-D model with 3-D crust (Chen et al. 2015a; Zhu et al. 2017), a hybrid model combining 3-D regional mantle and crustal models (**?**Krischer et al. 2018), or a combination of previous regional FWI models (Yuan et al. 2014; Tao et al. 2017). However, these initial model selections are not systematically discussed while lacking quantitative evidences on the models performance on different misfit functions. The contiguous U.S. is one of the most instrumented continental-scale regions that are extensively investigated by many tomographic studies (Engdahl et al. 1998; Bedle & van der Lee 2009; Schmandt & Humphreys 2010; Lin et al. 2012, 2014; Pavlis et al. 2012; Porritt et al. 2014; Schmandt & Lin 2014; Yuan et al. 2014; Schmandt et al. 2015; Shen & Ritzwoller 2016; Buehler & Shearer 2017; Burdick et al. 2017; Zhu et al. 2017; Jiang et al. 2018; Krischer et al. 2018; Nelson & Grand 2018) with different datasets and tomographic methods. This provides us a good example of examining different regional and global models to discuss a standard for selecting initial models in terms of different kinds of misfit functions.

The difficulties of selecting a initial model lie on: (1) we do not know the ground truth of the model, thus it is hard to systematically evaluate which model is better; and (2) different models are based on different datasets and inversion methods, which cannot be compared directly. Therefore, we start from the data-driven analysis, which is to compare the synthetic waveform predicted by different models with the observations, since a good model should be able to predict the observations well. Various model quality assessments for different regions have been performed by comparing the observed data and synthetics using different forward methods

(Alex Song & Helmberger 2007; Qin et al. 2009; Bozdağ & Trampert 2010; Gao & Shen 2012, 2015). These comparisons suggest that traveltime tomographic models generally only recover the approximate pattern of wave speed variations but not the full contrast and thus are unable to reproduce waveform distortions (Alex Song & Helmberger 2007), while new tomographic models utilizing more data coverages and/or full waveform inversion methods tend to have better predictability of waveforms (Gao & Shen 2012, 2015). However, the performance of these models under an accurate forward solver with more realistic Earth's properties including attenuation, topography, gravity, ellipticity, etc. into consideration is still black-boxed. Such evaluation not only tells whether these models are fit for complex models towards realistic, but also serves as an indication for selecting initial model for FWI with realistic properties into consideration.

In this work, we evaluate several recent shear wave speed models spatially resolving the contiguous U.S. and surrounding region for systematically assessing the model predictability of the seismic waveforms with a uniform spectral-element-method (SEM) based wave equation solver SPECFEM3D_GLOBE (Komatitsch & Tromp 2002a,b) with the consideration of attenuation, topography, gravity and Earth's ellipticity. In order to assess the model predictability, we investigate multiple misfit functions widely used in FWI approaches, including the travel time misfit, amplitude misfit, waveform misfit and the normalized zero-lag cross-correlation coefficient (NZCC) misfit for both body- and surface-waves on three components. These assessments can indicate the predictability in terms of different misfit functions, which bring out the models' performance on different aspects in terms of travel time, amplitude or waveform fitting. Especially, the NZCC is sensitive to both seismic phase arrival time match and waveform similarity between data and synthetics, which is more indicative of the model predictability of tomographic model than the commonly used criterion of travel time misfits derived from cross correlation. In the following sections, firstly, we summarize the seismic models selected for validation and discribe the SEM mesh implementation of different models in detail. Then we systematically compare measurements of different misfit functions for different models in three different period ranges, 9-20 s, 20-40 s, and 40-120 s, and discuss the model discrepancies accordingly. Lastly, we discuss the initial model selection for future FWI-based refinement.

2 DATA AND METHODS

2.1 Seismic models for assessment

Eight publicly available seismic models that have the resolution for the contiguous U.S are selected, including a differential travel-time tomographic model US-SL-2014 (Schmandt & Lin 2014), an ambient noise and receiver function joint-inverted model US.2016 (Shen & Ritzwoller 2016), two full-waveform inversion models SEMum-NA14 (Yuan et al. 2014) and Krischer18 (Krischer et al. 2018) constrained by long-period waves, and three global tomographic models GyPSuM (Simmons et al. 2010) inverted from travel times and geodynamic constrains, S362ANI and S40RTS (Kustowski et al. 2008; Ritsema et al. 2011) constrained by travel times, long period body waves and surface wave dispersions. The global 1-D model AK135 (Kennett et al. 1995) is also implemented as a reference and compared with the 3-D models. The used datasets and tomographic inversion methods for each model are briefly summarized in Table 1.

All seven 3-D models show similar large-scale pattern of shear wave speed anomalies in the upper mantle (Fig. 1), i.e., relatively low wave speeds (low-V) in the western U.S. and relatively high wave speeds (high-V) in the central and eastern U.S. However, the small-scale anomalies of tens or hundreds of kilometers differ dramatically in terms of not only the anomaly pattern but also the amplitude, which are caused by different datasets and methods used in the tomographic studies. For example, models US-SL-2014, US.2016, and Krischer18 clearly capture the Yellowstone hotspot in the northwestern U.S., while the other three miss this small-scale feature possibly due to the lack of resolution because of either sparse data coverage or long-wavelength seismic waves used in the inversion. It is notable that the full waveform inversion model Krischer18, although derived from long-wavelength seismic waves, can already capture small-scale structures such as the Yellowstone hotspot track. This further indicates that the full waveform inversion has the advantage of achieving sub-wavelength resolution (van der Kruk et al. 2015). However, in the case of lacking high-frequency data coverage, the full waveform method is less able to recover some small-scale structure compared to the inversions with traditional asymptotic methods but with more suitable datasets. For example, in Pacific Northwest, the Cascadia slab shows up as elongated narrow and strongly high-V anomalies in model US-SL-2014 because short-period teleseismic body wave travel time data enhances the sensitivity of such a scale. On the other hand, the FWI model Krischer18, although based on a more accurate 3-D sensitivity kernel, does not well capture the narrow high-V Cascadia slab due to the lack of short-wavelength teleseismic data that can sample the slab with good azimuth and incidence angle coverage.

Besides the differences in datasets and tomographic methods, crustal models used in the seismic inversion can also lead to dramatic differences between mantle models. An accurate crustal model is critical for correctly recovering deeper structure, especially the uppermost mantle which is more sensitive to the tradeoff with the wave speeds in the crust. The models selected for validation have large differences amongst the crustal models used in or resulted from their inversions. Figure 2 shows the absolute shear wave speeds at 20 km depth for three different crustal models resulted from inversions of models GyPSuM, US.2016, and Krischer18, along with the widely used 3-D crustal model, CRUST1.0 (Laske et al. 2013). The average shear wave speed difference amongst the crustal models within the contiguous U.S. reaches up to 10%, e.g., about 3.3 km/s beneath the Pacific Northwest in model Krischer18 compared to about 3.7 km/s in model US.2016, and an average of 3.5 km/s beneath the central and eastern U.S. in model Krischer18 compared to 3.9 km/s in model CRUST1.0. The impact of the crust and uppermost mantle on the predicted waveforms will be discussed in the following sections.

2.2 Spectral-Element Method and Model Implementation

The predictability of the selected 3-D models is evaluated by comparing the observed waveforms with the synthetic waveforms calculated by the SPECFEM3D_globe solver based on the spectral-element method (SEM) (Komatitsch & Tromp 2002a,b). The SEM combines the accuracy of pseudo-spectral method and the flexibility of finite-element mesh (Komatitsch & Tromp 2002a), which honors the topography/bathymetry and any laterally varying internal discontinuities of the Earth such as Moho, 410 and 660 discontinuities. It is more accurate in simulating surface waves than finite-difference methods which have stronger numerical dispersion issue (Robertsson 1996). The effects of Earth's ocean gravity, ellipticity, 3-D complex heterogeneity, attenuation, and anisotropy on seismic wave propagation can also be accurately modeled (Komatitsch & Tromp 2002b).

The SEM simulation mesh in this study is designed to simulate seismic waves accurately to the shortest period of 9 s, with a horizontal grid spacing of 5 km between Gauss-Lobatto-Legendre (GLL) points in the crust and doubled in the mantle. The computational domain is a spherical chunk from the surface to the core mantle boundary (CMB) spanning the entire contiguous U.S., Mexico, and majority of Canada, with horizontal dimensions of $48^\circ \times 48^\circ$

along great circles centered at (99° W, 30° N) and rotated by 30° counterclockwise (Fig. 3a) with Stacey absorbing boundary condition applied at the edges of the computational domain.

In order to compare the predictability of the 3-D seismic models into one uniform framework, we use the same SEM mesh configurations despite their differences in model parameterization, spatial coverage, grid size, and resolution. We ensure the mesh is sufficiently dense to capture the wave speed variations of all the 3-D models in their resolved regions. Each model is implemented with the following steps to honor the original 3-D wave speeds in its own model domain:

(1) All the models represented by wave speed perturbations are converted to the absolute wave speeds using the 1-D reference model provided by each tomographic study.

(2) For the simulation domain outside the model coverage, models CRUST1.0 and AK135 are implemented in the crust and mantle, respectively. The Moho interface is honored by the SEM mesh for the crustal model used such as model CRUST1.0 and a crustal model derived from model US.2016.

(3) For unconstrained physical parameters in any of the models, they are given the values according to the following: density (ρ) values of AK135 and CRUST1.0 are implemented in the mantle and the crust, respectively, for all models except model GyPSuM which has its own density model; V_p values of AK135 and CRUST1.0 are implemented in the mantle and the crust, respectively, for model SEMum-NA14; V_p values for model US.2016 are scaled from V_s in their study with a constant V_p/V_s ratio; V_{sh} and V_{sv} are given the same values of V_s for models US.2016, US-SL-2014, S40RTS and GyPSuM.

(4) In order to avoid any sharp discontinuities artificially introduced in merging different mantle and crustal models in the simulation domain, the models implemented on SEM mesh grids are smoothed with a 2-D Gaussian filter with a radius of 1.25° horizontally and 10 km in the mantle and 2 km in the crust vertically. Although the horizontal smoothing may alter some of the high-resolution models such as US.2016, the intermediate-period waveform (with periods longer than 10 s) do not change compared to the waveform calculated from the original model without smoothing (see appendix).

2.3 Validation dataset

A total of 30 earthquakes are selected from the global CMT solution catalog (Ekström et al. 2012) based on their large number of high-quality waveforms with high Signal-to-Noise Ratio (SNR) and representative geographic coverage of the simulation region (Fig. 3(a)). These events are from 2006 to 2019 with moment magnitude between 4.9 to 6.7. The depth of these events are mostly within the crust, and only two of them has the depth deeper than 30 km. 16 out of 30 events are located within the contiguous U.S. region. We used all the broadband stations available on IRISDMC with a total of 5,820, shown in Figure 3(c). In average there are more than 500 stations available for each event. To process the data, we first remove the instrument response and convert the records to displacement with a wide-band frequency taper as the pre-filter, and then check the data signal-to-noise ratio and select all traces with SNR>4. Then we band-pass filter the waveforms to our assessment frequency ranges with a zero-phase fourth-order Butterworth filter. Finally, both the data and the synthetics on E and N components are rotated to the radial and tangential (R and T) components according to the back azimuth. The synthetic waveforms follow exactly the same procedures of pre-processing as the data.

2.4 Misfit Measurements between Data and Synthetic Waveforms

We apply four different criteria in this study to evaluate the waveform fitting between the data and synthetics of different models: travel time misfit, amplitude misfit, least-squares waveform misfit, and the waveform similarity measured by the normalized zero-lag cross-correlation coefficient (NZCC). The travel time misfit for a single measurement is defined as the square of the travel time difference between data and synthetics measured by cross-correlation in the selected time window (Tromp et al. 2005):

$$\chi_r^T = \frac{1}{2}[T_r^s - T_r^d]^2, \tag{1}$$

where T_r^s and T_r^d are the measured travel time of the synthetics and data of a specific phase at station r. The amplitude misfit for a single measurement is defined as (Tromp et al. 2005):

$$\chi_r^A = \frac{1}{2}[A_r^d/A_r^s - 1]^2, \tag{2}$$

where A_r^s and A_r^d are the measured amplitude of the synthetics and data of a specific phase at station r. The waveform misfit for a single measurement is defined as (Tromp et al. 2005):

$$\chi_r^F = \frac{1}{2}\int_{t_s}^{t_e} [s(x_r, t) - d(x_r, t)]^2 \mathrm{dt}, \tag{3}$$

where $s(x_r, t)$ and $d(x_r, t)$ are the synthetic and data waveforms at the station r (with location x_r). t_s and t_e are the start and end time of the selected time window.

Besides these misfit functions, we also consider the normalized zero-lag cross-correlation coefficient (NZCC), which best reflects both the phase match and the complex similarity of waveform shape, e.g., triplicated waveforms but regardless of the absolute amplitude. It has been used as an objective function for full waveform inversion which robustly recovers seismic structures with strong wave speed contrasts (Liu et al. 2016; Tao et al. 2017, 2018). The NZCC is defined as:

$$\mathrm{NZCC} = \frac{\int_{\mathrm{t_s}}^{\mathrm{t_e}} \mathrm{s(x_r,t) \cdot d(x_r,t)dt}}{\sqrt{\int |\mathrm{s(x_r,t)}|^2 \mathrm{dt} \int |\mathrm{d(x_r,t)}|^2 \mathrm{dt}}} \tag{4}$$

where $s(x_r, t)$ and $d(x_r, t)$ are the multi-component synthetics within the measurement time window at station r. For the P, SV and Rayleigh waves, the vertical (Z) and radial (R) components are used for calculating NZCC, while for the SH and Love waves, only the tangential (T) component is used.

It is important to assess the models in representative frequency ranges because different frequency ranges of body waves and surface waves are sensitive to different scales of structure and depth, respectively. It is also meaningful to assess whether the models have ability to predict waveforms out of their inverted frequency range. Considering most of the long period tomographic models (e.g., SEMum-NA14 and S40RTS) are started from 40 seconds, we choose 9-20 s, 20-40 s and 40-120 s to separate three different representative frequency ranges, which shows the predictability of short-, intermediate- and long-period waves.

To allow a fair comparison, we select time windows for different seismic phases according to the empirical travel time of the P and S phases calculated by 1-D model AK135, and the empirical travel time of the Rayleigh and Love waves using constant velocities for each period ranges (Table 2.) For intermediate period waves, S waves are not well separated from the surface wave train in local epicentral distances ($\Delta < 10°$). Therefore, for local epicentral distances ($\Delta < 10°$), only P(Pnl) and Surface wave windows are selected, yet P, S, and surface wave windows for $\Delta \geq 10°$ are selected. The P and S windows are selected 10 s before and 60 s after the empirical arrival time. On the other hand, the surface wave windows are 10 s before and 120 s after the empirical arrival time of the surface wave train. The measurement windows are then fine selected by the following criteria: 1) the signal-to-noise ratio of the data (SNR>4) and 2) the cross-correlation coefficient of the data and synthetics (CC>0.7).

The total misfit function for a model combines all the measurements for selected measurement windows for each event-station pair. We apply the same weighting scheme as previous FWI works (Tape et al. 2010; Chen et al. 2015a; Zhu et al. 2017) to make our model assessment consistent with FWI workflow thus the result is representative for initial model selection. Such weighting scheme includes categorical weighting (Tape et al. 2010; Chen et al. 2015a; Zhu et al. 2017), which separates all the measurements to six categories: body wave and surface wave on Z, R and T components. This scheme balances different number of measurements on each components and seismic phases. Since the station distribution is highly biased and varies for different events (e.g., a dense local network with 10-km station spacing such as SCEDC, compared to the USArray with average station spacing of 50–80 km), it is important to apply a proper weighting scheme to account for the biased station distribution for each event in evaluating the overall predictability of each model. For each testing event, we applied the station weighting based on their geographical distribution (Ruan et al. 2019). To make the measurements of different windows comparable, we normalize the travel time misfit and the amplitude misfit by the standard deviation of their measurement, i.e.,

$$\chi^T = \frac{1}{2CN} \sum_c^C \sum_r^N W_c W_r \left(\frac{T_r^s - T_r^d}{\sigma_r} \right)^2, \tag{5}$$

$$\chi^A = \frac{1}{2CN} \sum_c^C \sum_r^N W_c W_r \left(\frac{A_r^d / A_r^s - 1}{\sigma_r} \right)^2, \tag{6}$$

where W_r is the geographical station weighting coefficient (Ruan et al. 2019) and W_c is the category weighting coefficient, which is the inverse of the number of all the selected measurement time windows of that category. σ_r is the estimated error of the measurement, calculated by the MEASURE_ADJ (Tape et al. 2009). In the waveform and NZCC measurements, since it is ambiguous to define the standard deviation of the measurement, we only apply the categorical and geographic weighting:

$$\chi^F = \frac{1}{CN} \sum_c^C \sum_r^N W_c W_r \chi_r^F \tag{7}$$

$$\chi^{\mathrm{NZCC}} = \frac{1}{CN} \sum_c^C \sum_r^N W_c W_r (1 - \mathrm{NZCC}) \tag{8}$$

where W_r and W_c are the geographical and categorical weighting, respectively.

3 RESULTS

3.1 Waveform Comparison of Different Seismic Models

Mantle model mainly affects regional epicentral distance body-wave recordings. We choose a profile of stations within a 20° aperture angle along the west-east great arc starting from the epicenter of event 201305240347A (Fig. 3(b)) to compare the waveforms on two short and intermediate period ranges (9-20 s and 20-40 s, Fig. 4 and 5). The epicentral distance of the recordings ranges from 5° to 33° (Fig. 3(b)). For short period range of 9-20 s, none of the models have high predictability of the waveforms. Among the models, S40RTS and US-SL-2014 are relatively better at predicting the shear wave on vertical and radial components at larger epicentral distances, followed by model US.2016. For some stations the waveform is relatively complicated, which might be related to local structures, i.e., basins. On tangential component, the result is relatively similar but model S362ANI and SEMum-NA14 performs better. In 20-40 s period range, all testing models are experiencing great improvement for predicting the shear wave and predicts three components in larger epicentral distance quite well. However, the very low shear wave amplitude in epicentral distance around 12-15 degrees related to the SV-wave nodal plane are not well predicted by any of the models due to the possibly inaccurate source parameters. More waveform comparisons along the same trace but with longer (40-120 s) period range are even improved, and shown in the appendix.

Short-period surface wave has high sensitivity in the crust. For example, Rayleigh wave in period range of 9-20 s is most sensitive to upper to middle crust structure. While intermediate period range, i.e., 20-40 s, is more sensitive to the lower crust and uppermost mantle velocity structure. Fig. (6) and (7) show the comparison of short (9-20 s) and intermediate (20-40 s) period Rayleigh and Love waves, respectively. We only show models with different crust because for all models with Crust1.0, the synthetic Rayleigh and Love waves in such period ranges have little difference. At some epicentral distances, e.g., 20-30°, the short period Rayleigh and Love waveforms are relatively complicated with strong coda waves, which may related to reverberations triggered by the deep sedimentary basins (e.g., Forest City, Cherokee and Illinois) (Coleman Jr & Cahan 2012) (also see appendix). It looks that none of the models can predict the complicated short-period coda waves, however, model US.2016 and AK135 are relatively better at predicting Rayleigh waves in Z and R components, and GyPSuM is significantly better in predicting Love waves. Also, strong cycle-skipping effect can be observed in most of the models. In intermediate period range (20-40 s), almost all the models can significantly better predict the waveform. However, cycle-skipping, although mitigated, can still be observed especially in Crust1.0 and Krischer18. The first coming wave train with longer period are less fitted compared to the later wave train. Model GyPSuM is still the best at predicting Love waves.

More waveform comparison results are plotted in Appendix A1 and A2. We observe a generally trend that almost all the models predict the waveform better in lower frequency range (e.g., 40-120 s). The surface wave cycle skipping effect is also mitigated. We notice that the current models can predict long wavelength body and surface waves quite well, however, the predictability for short-period body waves especially surface waves still needs improvement. The shallow structures especially basin structures are not yet constrained.

In the following sections, various statistic analysis are performed for further assessment of each model and selection of initial model for FWI.

3.2 Statistical result of waveform similarity and misfits

Travel time shift distribution of all the measurements is a straightforward statistical criteria and directly indicates the mean velocity and the deviation of each models, where positive or negative travel time indicates advancing or delay of the synthetics compared to the observations, implying that the wave speed models are either faster or slower compared to the ground-truth models. The overall travel time shift distribution of all the measurements (Fig. 8) are plotted for each model in three period ranges. We observed that model S40RTS and S362ANI have the minimum standard deviation in all three period ranges, indicating these two models are able to predict the travel time well for most of the measurement windows with less large-error outliers compared to other models. Model GyPSuM, Krischer18 and US.2016 has the lowest mean travel time error for 9-20 s, 20-40 s and 40-120 s, respectively. It is possible that these models have better average velocity at those frequency ranges compared to other models. All the models have a negative mean travel time shift in 9-20 s and 40-120 s, while only GyPSuM and Krischer18 have positive travel time shift in 20-40 s period range. This observation reveals that most of the current models have slightly slower mean shear wave speed in the contiguous U.S and surrounding regions compared to the ground truth. Measurements with only body waves and surface waves share similar statistical result (Figs. A4 and A6 in the appendix). SH wave speeds for all the models seem to systematically slower (Figs. A5 and A7 in the appendix), while models SEMum-NA14 and S362ANI are better, which is because these two models have radial anisotropy in constrain.

Misfit functions define the overall model predictability in a more straightforward way. In Fig. 9, we plot travel time misfit, amplitude misfit, waveform misfit and NZCC misfit for all models in three period ranges. The travel time misfit and NZCC misfit share similar trend of model ranking, which is because of the NZCC misfit measures the phase difference which is coherent to the travel time misfit. Models S40RTS, S362ANI and US.2016 are the top three models with minimal overall travel time misfit and NZCC misfit in 20-40 s and 40-120 s period ranges, while in 9-20 s period range, model AK135 takes the place of US.2016. It seems that global models constrained by both the travel time data (short period) and surface wave dispersion data (long period) has the smallest misfit of phase for both the body and the surface wave in different frequency ranges. For the amplitude and waveform misfit, we can observe that with the period range getting larger, both the amplitude and waveform misfit are approaching a similar trend of model ranking as travel time and NZCC misfit, while in short period range the amplitude and waveform misfit are more scattered. The amplitude and waveform misfit may not be very indicative because none of the tested models are inverted using constrains from absolute amplitude or least squares of waveform. The short period surface wave may suffer from severe cycle skipping effect, which can significantly enlarge the waveform misfit. Besides, the complicated coda waves possibly related to small-scale heterogeneities in the crust or the sedimentary basin makes it harder for models to predict the absolute amplitude and waveform in short period. In long period range, both the cycle skipping and the effect of sedimentary layer are mitigated, which makes the amplitude misfit and waveform misfit more indicative. Therefore, model US.2016 and SEMum-NA14 might be better to predict more accurate absolute amplitude and waveform in 40-120 s period range. Further refinement for near-surface small scale heterogeneities is still needed for seismic wave speeds models of contiguous U.S and surrounding regions.

Using NZCC, we can measure how many percentage of windows are selected for measurement from all the windows. It is an important criteria that straightforwardly indicates the number of available measures we can obtain in typical FWI process, thus indicative for initial model selecting. Here, we plotted the percentage of NZCC>0.7 for all the models in three period ranges and 6 categories (Fig. 10). To make a fair comparison, we examine only contiguous U.S. earthquakes including events offcoast western U.S because models US.2016 and US-SL-2014 only have contiguous U.S part resolved. For short (9-20 s) period range, models S362ANI, S40RTS and GyPSuM are the three better models with higher percentage of good measurement windows of body waves, while model US.2016, US-SL-2014 and Krischer18 have higher percentage of good Rayleigh waves. For love wave, model AK135+Crust1.0 takes the place of model US.2016, which indicates that Crust1.0 may have a better constrain on short period SH wave speeds. For long (40-80 s) period ranges, models S40RTS, S362ANI and SEMum-NA14 are the top three models with the highest percentage of all 6 categories of waveforms, which indicates that models with long period waveform incorporated in the inversion will be good at predicting long wavelength seismic waveforms. In the intermediate (20-40 s) period range, models S40RTS and S62ANI are among the best three models with the highest percentage of NZCC>0.7 for all the categories, while SEMum-NA14 and Krischer18 are also good for some categories. A clear trend that the overall percentage of good measurements increases with increasing period range.

The model predictability varies with the epicentral distance in each category (Fig. 11). For surface waves, the predictability of all the models worsens with increasing epicentral distances.

This may due to the small-scale heterogeneities in the crust and uppermost mantle are not well captured by the models which can not reproduce the more complex surface wave dispersion at increasing epicentral distances. There is no clear dependance of model predictability of body waves (P-SV and SH) with epicentral distances. For specific models, model AK135 predicts 9-20 s shear wave in short epicentral distance well, however adding Crust1.0 even worsened the result, which indicates that for local continental crust and uppermost mantle structure, AK135 is a good 1D reference model. When the epicentral distance increases, models S40RTS and S362ANI shows better predictability. Model US.2016 predicts short period Rayleigh wave especially very well in almost all the epicentral distances, however, for Love wave, models with Crust1.0 performs better. In 20-40 s period range, model S40RTS and S362ANI predicts the body waves better, while for surface waves, models Krischer18 and SEMum-NA14 becomes better especially in longer epicentral distances. Models S40RTS and S362ANI also best predicts long period (40-120 s) body and surface waves, while Model S362ANI is better for SH and Love waves, because it has transversely isotropy inverted. Models SEMum-NA14 and GyPSuM are also among the highest predictability in long period SH and Love waves.

4 DISCUSSION

A fair comparison of models need to consider the complexity of model inversion process, including the data coverage, frequency range, model parameterization, and inversion scheme, etc. Since many models only have mantle structure inverted with limited depth ranges, e.g., SEMum-NA14 from 60 to 410 km, we need to attach reference models to create the mesh. Therefore, understanding the waveform comparison result need to be careful. For example, only intermediate-long period surface waves and certain epicentral distance (about 10-30°) are sensitive to the upper mantle region which most models have the best resolution. We take special notice to these issues by analyzing the percentage of waveforms with NZCC greater than 0.7 with respect to the epicentral distance in different frequency ranges.

The complexity of 3-D wave propagation effects, including multi-phase, multi-pathing, and scattering induces difficulty to the waveform comparison. For example, the S-wave and Rayleigh wave are not well separated for the epicentral distance about 5-10° in the period ranges of this study. In this case, the short period surface wave (sensitive to crustal structure) and body wave (sensitivity depth about 42-66 km) are mixed together. With this limitation, the waveform fitting comparison is not likely to distinguish the performance of crustal and mantle models, instead, the compatibility of crustal and mantle models matter for a hybrid model (e.g., mantle models with CRUST1.0 on top). This limitation will be mitigated in higher frequency, i.e., shorter wavelength. Therefore, pushing the shortest resolvable period higher is very important for not only model assessment but also the inversion.

Overall, in longer period range, each model has higher and similar level of waveform predictability in terms of both NZCC and travel time, which is consistent with the coherent large-scale structure of different models. In short period range, the predictability decreases and varies, which is related to the discrepancies of small-scale structures. Models with specific dataset will significantly improve the predictability within that category. For example, model US.2016 with short period Rayleigh wave dispersion data recorded by USArray significantly improves the fitting of 9-20 s Rayleigh wave, resulting in a better crustal isotropic shear wave velocity model. Models Krischer18 and SEMum-NA14, both FWI models with long period (30-40 s) body and surface waves, are able to predict the long period (40-120 s) validation datasets and even for the intermediate period (20-40 s). It is a result from the FWI approach utilizing the most information on the phases of the seismic waveforms, which may have sub-wavelength resolution (van der Kruk et al. 2015). It is noticeable that global models (S40RTS, S362ANI and GyPSuM) performs well in terms of predicting phase related observables (i.e., travel time and NZCC) in all three frequency ranges, even though they are not resolving small scale heterogeneities. It is reasonable because all those global models are constrained by mutiple datasets, including travel time, long-period body wave, and surface wave dispersion data. The body wave travel time ,although based on ray-theory approximation and suffering from wavefront healing effect that reduces the amplitude of the wave speed anomaly thus lowers the resolution (Montelli et al. 2004), still helps constrain high-frequency components in terms of the phase of seismic waves. Therefore, with both high frequency and long period datasets, these global model are able to have a good waveform predictability. The relatively evenly distributed earthquake and station locations in global model inversions may also help to balance the sensitive kernel of different geographical region and difference depth, which helps reduce the bias of the model. This observation also suggests that a model with better fitting of the phase of seismic waveform is more likely have reliable large-scale structures and may not necessarily have better small-scale structures resolved. This observation indicates that combining unbiased multiple measurements and datasets are critical for seismic wave speeds inversion. For a regional study, special attention should be paid to the possible unevenly distributed source and stations and a proper weighting scheme should be applied to mitigate the bias.

Since all models assessed are inverted from the phase (travel time, dispersion, etc.), it is reasonable that the absolute amplitude and L2 norm of the waveform are not well minimized yet, resulted in the unstable testing result for amplitude and waveform misfit. Besides, the model attenuation also influences the absolute amplitude and waveform, which is also not constrained by any models. It is also observed that sedimentary basins may produce strong reverberations thus resulting in complicated waveforms which are not able to be predicted by any models. Radial anisotropy is also not well constrained except for the two models which already taken them into account. Therefore, a further model refinement for the contiguous U.S and surrounding regions aiming at short-wavelength and radial anisotropy in crustal and upper mantle is still very useful. Since we still observe discrepancies of waveform predictability in long period (40-120 s), it is still necessary to start from long period range to refine large-scale models, and higher frequency body and surface waves are also highly needed to be later incorporated to constrain small-scale heterogeneities in both mantle and crust.

The crustal model has significant influence not only on short period surface waves, but also on long period body waves. It is reported that for travel times measured in long periods, although mostly sensitive to mantle structure, are seconds different than the ray-theory prediction, which is related to the crustal effects (Ritsema et al. 2009). In this work we also observed that different mantle models seem to be compatible with different crustal models, i.e., models S40RTS and S362ANI are in good agreement with model Crust1.0, resulting in a better predictability. It is very important to obtain good crustal models for further refining the mantle model.

Finally we would like to give an overall evaluation for different models. Model S40RTS and S362ANI perform overall the top two in predicting both the body waves and long period surface waves, indicating that the shear wave speeds in these models are well constrained in the mantle, which may be benefited from high-quality and spatially balanced global measurements as well as multiple phases sensitive to both the upper and lower mantle structure. Model US.2016 is the best model to predict the Rayleigh wave especially in the short period range. However, model US.2016 performs less well than the S40RTS+Crust1.0 in predicting the shear waves. Because AK135 is implemented along with US.2016 beneath 150 km depth where US.2016 has no coverage, it is reasonable that the body waveform fitting is not ideal especially for body waves that penetrate through deeper mantle structure. Models SEMum-NA14, GyPSuM and Krischer18 are also good at long-period range waveform fitting. Especially for model SEMum-NA14, it predicts short epicentral distance SH and Love wave in 40-120 s the best, which benefits from the transversely isotropic parameterization applied in the model. For the crust, model Crust1.0 has lower predictability than US.2016 in SV and Rayleigh waves, however it predicts SH and love waves well. All these observations suggest the commonly used FWI starting model S362ANI+Crust1.0 is reasonable. Moreover, a hybrid model combining surface-wave-tomography-constrained crust (i.e., US.2016) for V_{SV} and Crust1.0 for V_{SH}, and global model (i.e., S40RTS or S362ANI) for the mantle will possibly work better in terms of more available measurements and better initial waveform fitting, which is likely to be closer to the global minimum and more suitable for further FWI model refinement.

5 CONCLUSION

By analyzing the travel time misfit, normalized zero-lag cross-correlation coefficient and percentage of high waveform coherence measurement windows, we found that the optimized seismic models for the contiguous U.S and surrounding region in the mantle are the global models with unbiased datasets (S40RTS or S362ANI); while in the crust are the surface-wave-tomographic model US.2016 (for V_{sv}) and CRUST1.0 (for V_{sh}). It is noticeable that tomographic models best constrain the sensitivity range of their data sets. Besides, the current tested models have large discrepancy of waveform predictability especially in short period range (9-20 s), which results from the incomplete constrain of the small-scale heterogeneities in the crust and upper mantle, especially the shallow basins. The radial anisotropy for crust and uppermost mantle is yet not well constrained. Therefore, a further refinement of the wave speeds model of contiguous U.S and surrounding regions is critical for better constraining the contiguous U.S region and further geological understandings. A hybrid initial model combining S40RTS or S362ANI in the mantle and US.2016 for V_{sv} and CRUST1.0 for V_{sh} in the crust will be suitable for the FWI-based refinement in terms of better initial data misfit and more numbers of high-quality measurements.

ACKNOWLEDGMENTS

Models GyPSuM, SEMum-NA14, US-SL-2014, US.2016, S362ANI and AK135 are downloaded from the website of the Incorporated Research Institutions for Seismology (IRIS) Earth Model Collaboration (EMC) (http://ds.iris.edu/ds/products/emc/). Models S40RTS and Krischer18 are provided by Ritesma et al., (2011) and Krischer et al., (2018). Model CRUST1.0 is downloaded from the REM website (https://igppweb.ucsd.edu/ gabi/crust1.html). Seismic data are downloaded from the International Federation of Digital Seismograph Networks (FDSN, https://www.fdsn.org), Canadian National Seismic Network (CNSN, http://www.earthquakescanada.nrcan.gc.c
and Servicio Sismológico Nacional (SSN, http://www.ssn.unam.mx). The earthquake CMT

solutions are from the global CMT webpage (https://www.globalcmt.org). The open-source spectral-element software package SPECFEM3D_GLOBE and the moment-tensor inversion package CMT3D used for this article are freely available for download via the Computational Infrastructure for Geodynamics (CIG, https://geodynamics.org). Digital data of outlines of LIPS and hotspot locations are downloaded from http://www-udc.ig.utexas.edu/external/plates/data.htm. We thank Lion Krischer, Scott Burdick, and Incorporated Research Institutions for Seismology (IRIS) EMC for providing all the tomographic models. We also thank Lion Krischer, Andrew J. Schaeffer, Xyoli Pérez-Campos, and Robert Herrmann for their constructive discussion and suggestion regarding seismic model implementation or data acquisition. The seismic waveform data were downloaded from IRIS Data Management Center. We thank the Institute for Cyber-Enabled Research (ICER) at Michigan State University and the Extreme Science and Engineering Discovery Environment (XSEDE supported by NSF grant ACI-1053575) for providing the high-performance computing resources. This research was supported by NSF grant 1802247 and the startup fund of Min Chen at Michigan State University.

Table 1. Summary of the seismic models for validation

Models	Measurement	Dataset and frequency range	Model coverage
AK135	TT	Global stations before 1995	Global V_p, V_s, ρ
CRUST1.0	SF, RF, ACT	Global stations before 2013	Global layered crust V_p, V_s, ρ and Moho depth
GyPSuM	TT, GRA, GD	Global stations 1964-2007, 14-100 s	Global V_p, V_s and ρ, 0-2900 km
S40RTS	TT, SF, NM	Global stations before 2011	Global V_p, V_s, and ρ
US-SL-2014	TTR	USArray, NCEDC, SCEDC, 2011-2014, 1-20 s	$\delta\mathrm{lnV_p}$ and $\delta\mathrm{lnV_s}$, Contiguous U.S., 60-1220 km
SEMum-NA14	FWI, NM	USArray, North America stations before 2013, 40-120 s	V_{sv} and V_{sh}, 10-80N, 30-330W, 50-410 km
US.2016	ANT, SF, HV, RF	USArray stationss, 2006-2016, 8-90 s	V_s and Moho depth, Contiguous U.S., 0-150 km
Krischer18	FWI	FDSN hosted stations, 2005-2016, 30-120 s	V_p, V_{sv} and V_{sh}, 0-1440 km, North America and North Atlantic
S362ANI	TT, SF, WF	Global stations from 1994-2003, 50-200 s for WF and 35-150 s for SF	V_{sv} and V_{sh}, 25-2890 km, Global

Abbreviations for types of measurements: ACT: Active source survey; ANT: Ambient noise; FWI: full waveform inversion; GD: Geodetic measurements; GRA: Gravity measurements; HV: H/V ratio (Rayleigh wave ellipticity); NM: Normal mode; RF: Receiver function; SF: Surface wave dispersion; TT: Travel time; TTR: Travel-time residuals; WF: Waveform inversion using path average approximation.

Abbreviations for model velocities: V_s: shear wave speed; V_p: P-wave speed; V_{sh} horizontally traveling and horizontally polarized shear wave speed; V_{sv}: horizontally traveling and vertically polarized shear wave speed; Q: quality factor; ρ: density; δlnV: percentage perturbations relative to a 1-D reference model.

Network abbreviations: NCEDC: Northern California Earthquake Data Center, SCEDC: Southern California Earthquake Data Center, FDSN: International Federation of Digital Seismograph Networks

Table 2. Empirical surface wave speed for window selection

Frequency range	Rayleigh wave speed	Love wave speed
9-20 s	3.2 km/s	3.7 km/s
20-40 s	3.3 km/s	3.9 km/s
40-120 s	3.5 km/s	4.2 km/s

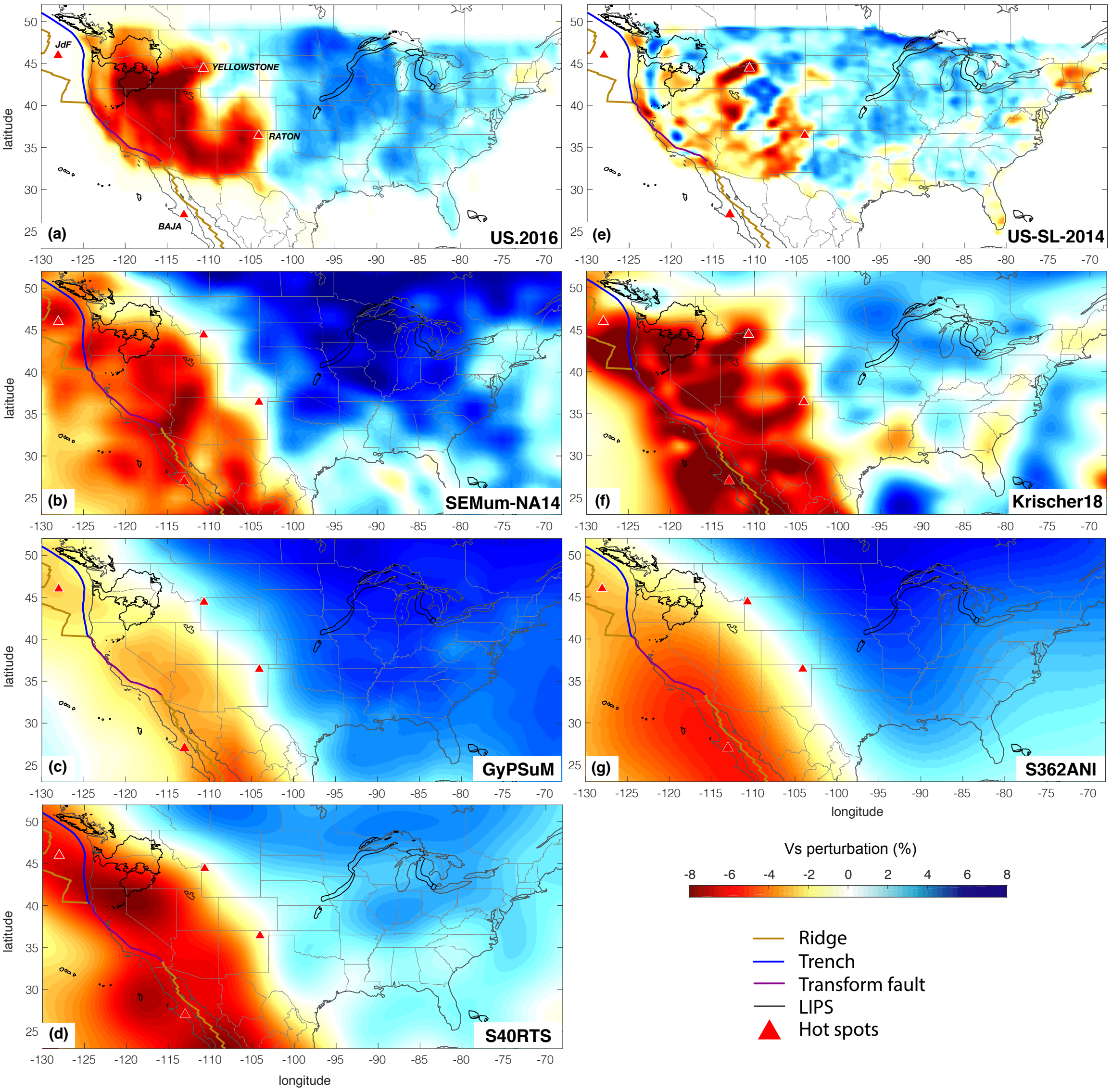

Figure 1. Comparison of seven shear wave speed models (US.2016, SEMum-NA14, GyPSuM, S40RTS, US-SL-2014, Krischer18 and S362ANI) beneath the contiguous U.S. at 100 km depth. Shear wave perturbations are relative to 1-D reference model AK135. For display purpose, all models are interpolated on even grids with a horizontal grid spacing of 0.25°. Models US.2016 and US-SL-2014 only cover part of the map region within the contiguous U.S. and the rest of the map is filled with zero shear wave speed perturbation. Plate boundaries and large igneous provinces (LIPS) are marked with colored lines. Red triangles denote the hot spots or volcanic regions beneath Juan de Fuca plate, Yellowstone, Raton-Clayton and Baja California (Coffin et al. 2005).

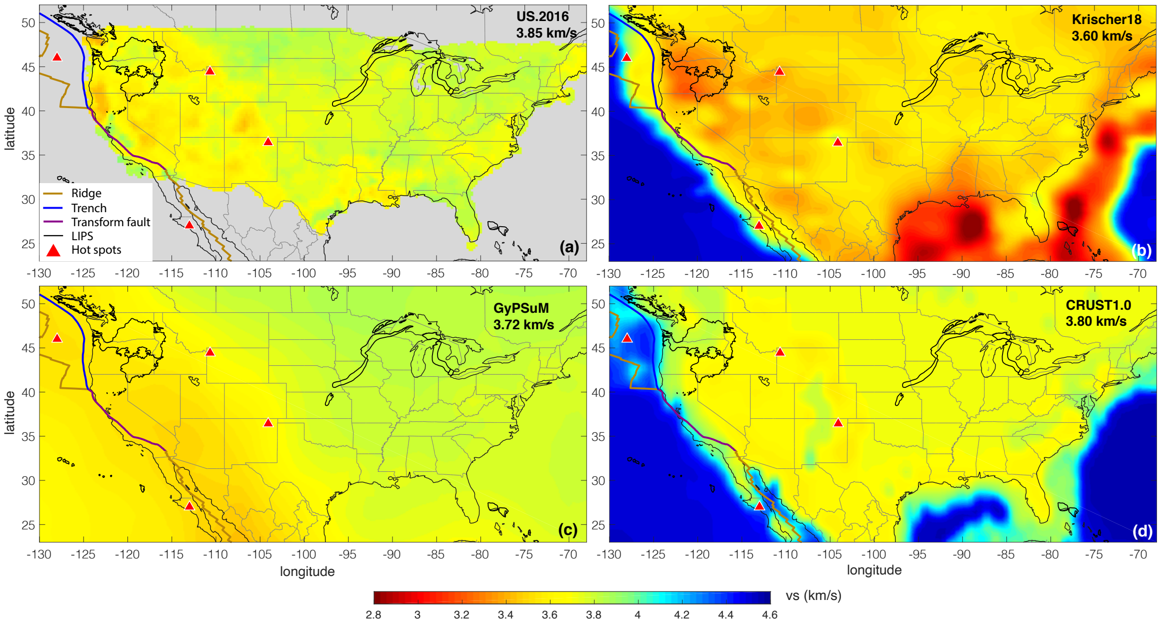

Figure 2. Maps of absolute shear wave speeds of the four selected crustal models at 20 km depth. (a) model US.2016; (b) model Krischer18; (c) model GyPSuM; (d) model CRUST1.0. Only models US.2016, Krischer18 and GyPSuM have crustal structure provided, all the other models are implemented with model CRUST1.0 in the crust. Model US.2016 only covers part of the map region and the rest is filled up with gray color. The plotting interpolation method and the marked geological units are the same as those in Figure 1.

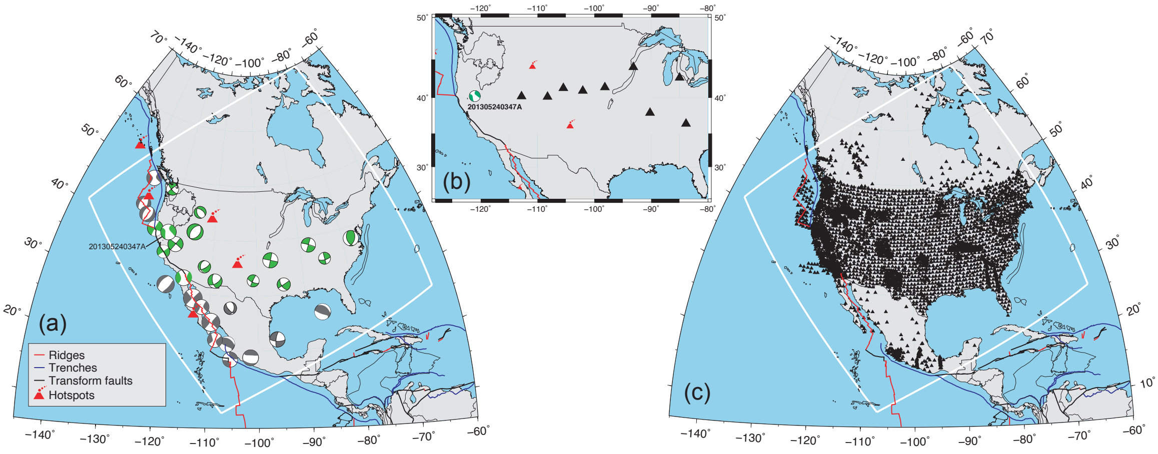

Figure 3. Event and station distribution in the simulation region. (a) The 30 selected events for waveform comparison. Green colored beachballs are contiguous U.S events, while dark gray colored beachballs are other events outside contiguous U.S. White box outlines the simulation region. (b) The earthquake 201305240347A for waveform demonstration, and the stations along a E-W profile with aperture angle of 20 degrees. (c) All the stations used for waveform comparison. The red line indicates the profile we used to compare waveforms.

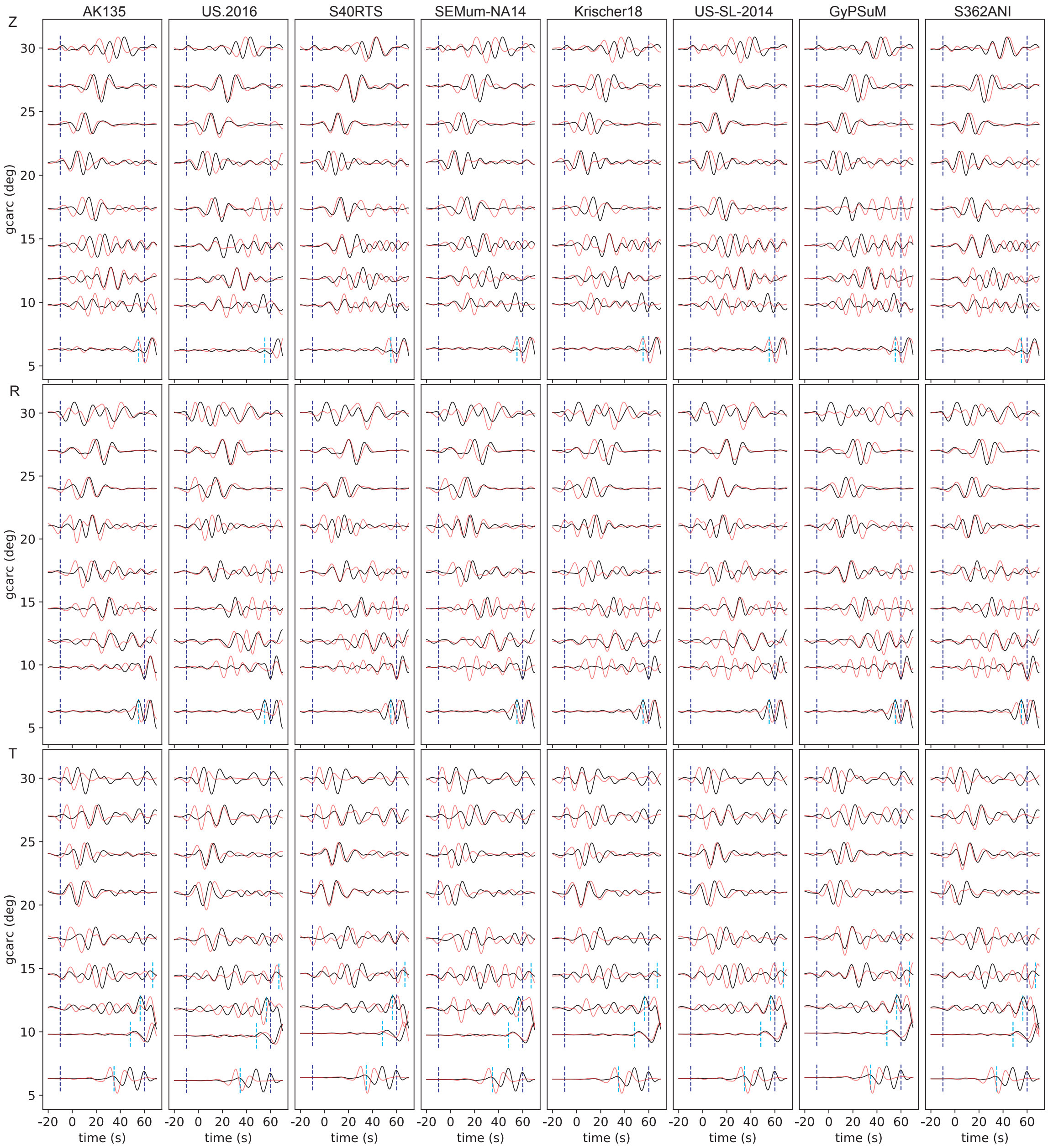

Figure 4. Waveform comparison for short period shear wave. The seismic recordings are filtered between 9–20 s and aligned with the theoretical arrival time of S-wave (time=0). Black and red lines are the observed and synthetic waveforms, respectively. Blue dashed lines mark the shear wave measurement window. Cyan dashed line indicates the starting of surface wave calculated by empirical surface wave speeds in Table. 2. For the station less than 5 degrees, surface wave components are incorporated in the measurement window. Models S40RTS, S362ANI, US-SL-2014, and SEMum-NA14 have Crust1.0 on top.

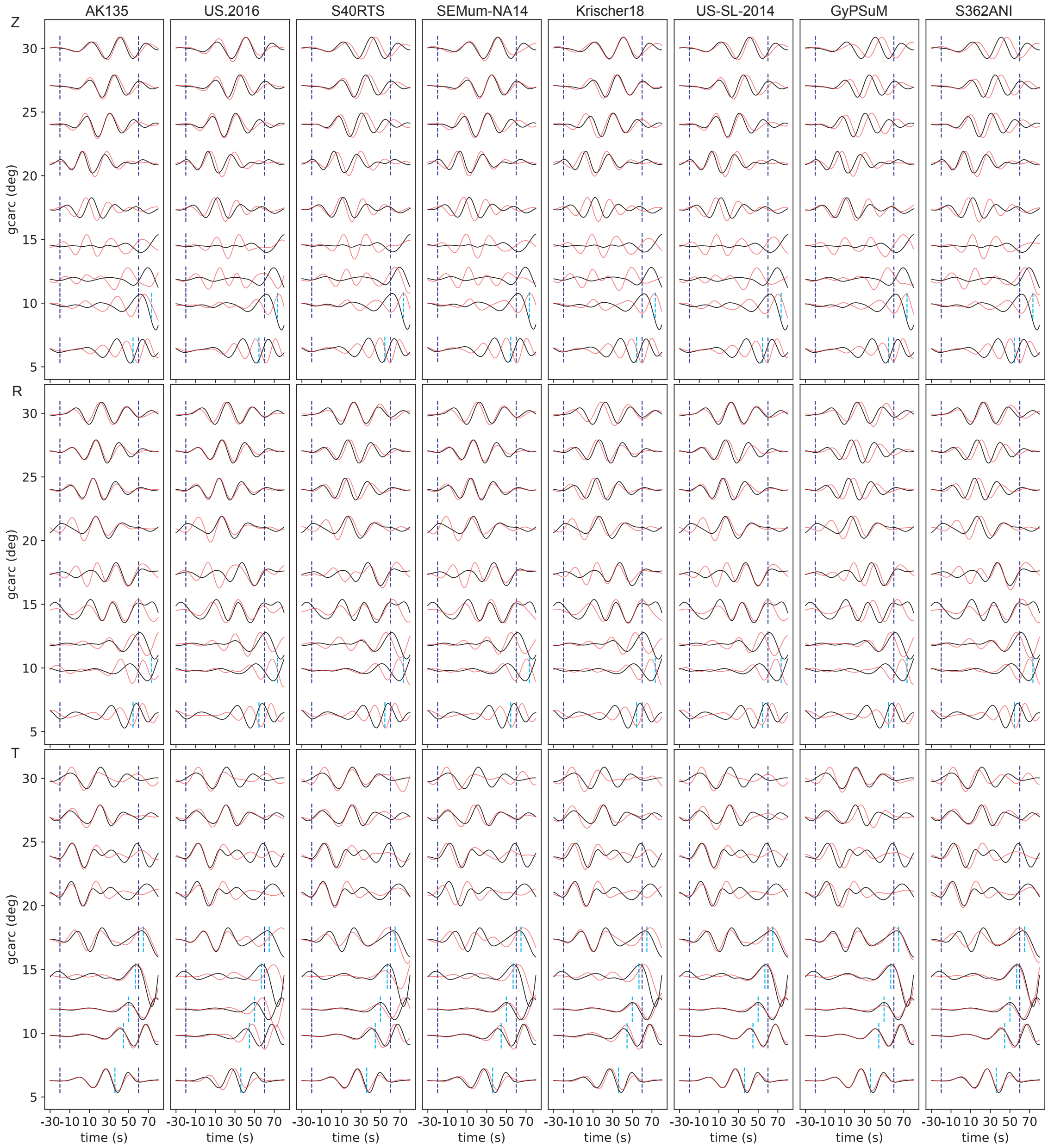

Figure 5. Waveform comparison for intermediate period shear wave. The seismic recordings are filtered between 20–40 s and aligned with the theoretical arrival time of S-wave (time=0). Black and red lines are the observed and synthetic waveforms, respectively. Blue dashed lines mark the shear wave measurement window. Cyan dashed line indicates the starting of surface wave calculated by empirical surface wave speeds in Table. 2. Models S40RTS, S362ANI, US-SL-2014, and SEMum-NA14 have Crust1.0 on top.

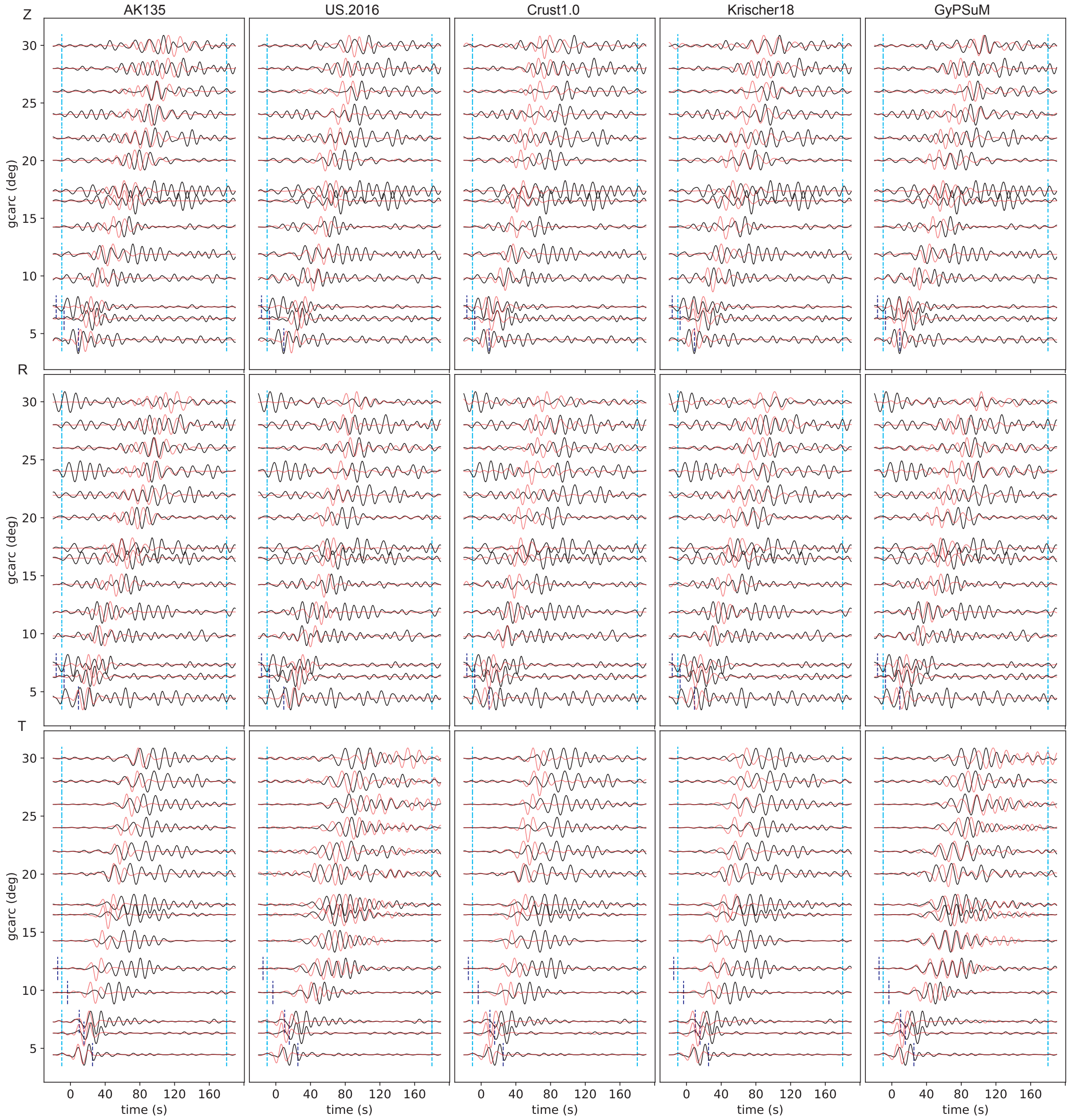

Figure 6. Waveform comparison for short period surface wave. The seismic recordings are filtered between 9–20 s and aligned with the empirical arrival time of Rayleigh or Love waves. Black and red lines are the observed and synthetic waveforms, respectively. Cyan dashed lines mark the surface wave measurement window. Blue dashed line indicates the end of shear wave calculated by 60 seconds after empirical S wave arrival time calculated by 1-D model AK135.

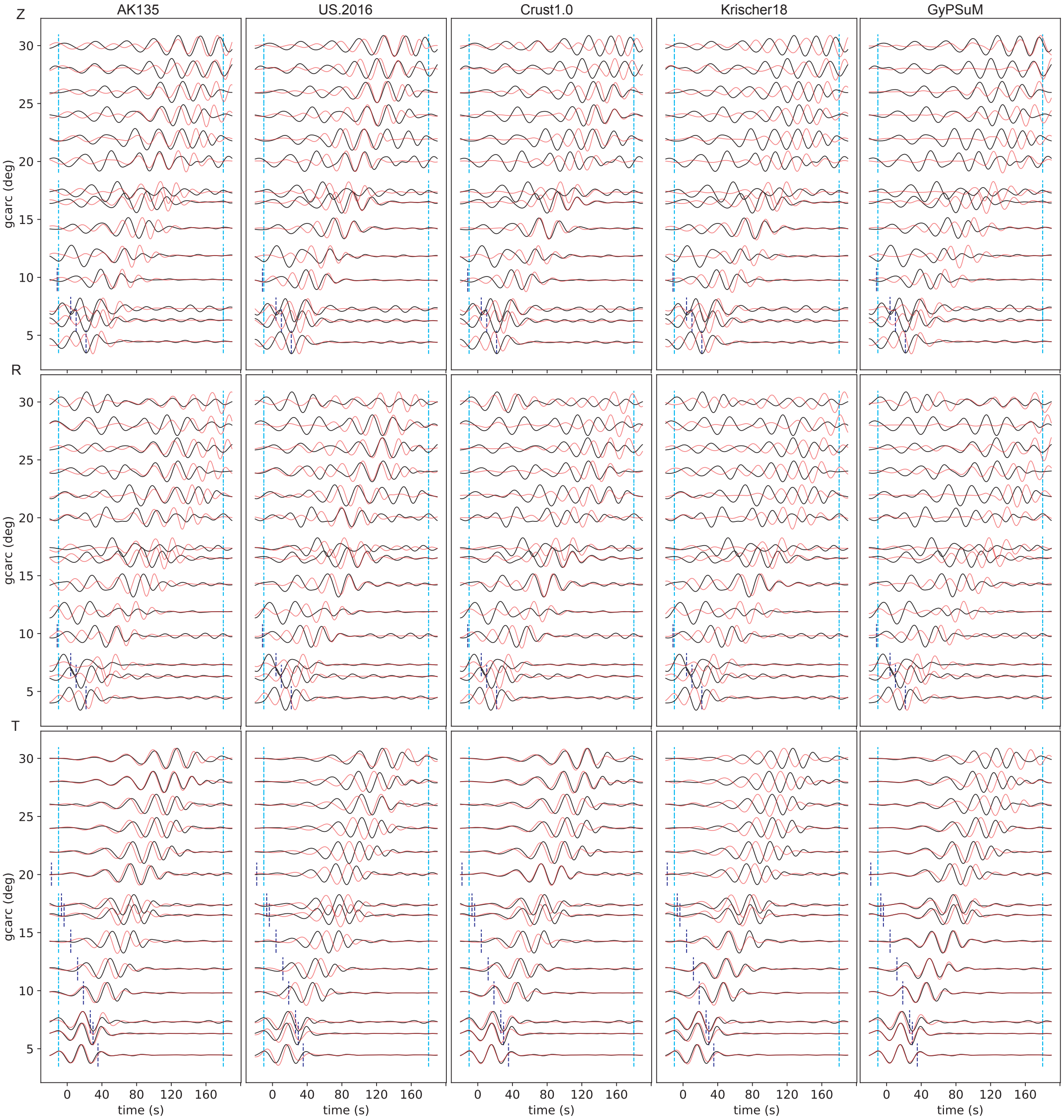

Figure 7. Waveform comparison for intermediate period surface wave. The seismic recordings are filtered between 20–40 s and aligned with the empirical arrival time of Rayleigh or Love waves. Black and red lines are the observed and synthetic waveforms, respectively. Cyan dashed lines mark the surface wave measurement window. Blue dashed line indicates the end of shear wave calculated by 60 seconds after empirical S wave arrival time calculated by 1-D model AK135.

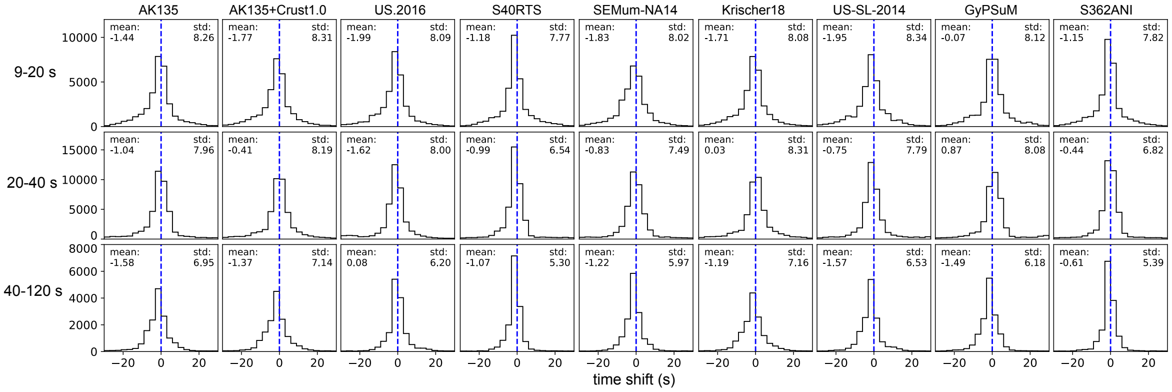

Figure 8. Travel time shift distribution histograms for overall measurement windows. Rows upper to lower: 9-20 s, 20-40 s and 40-120 s; Panels left to right: different models.

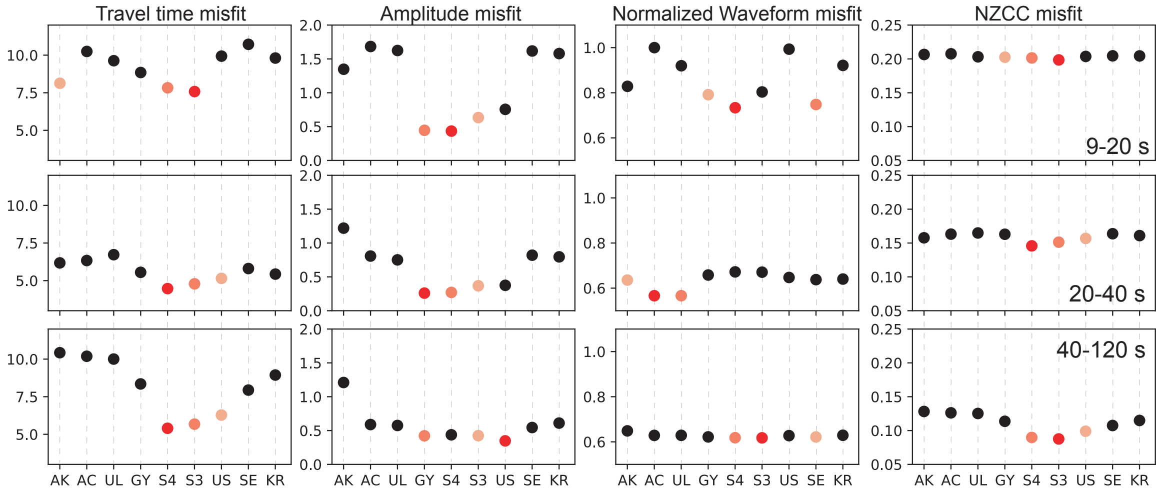

Figure 9. Four types of misfit for contiguous U.S events in three period ranges. Rows upper to lower: 9-20 s, 20-40 s and 40-120 s; Panels left to right: travel time, amplitude, waveform and zerolag CC misfits, respectively. First 3 models with minimum misfits are marked with different reds. The x-axis marks are for different models: AK: AK135, AC: AK135+Crust1.0, UL: US-SL-2014, GY: GyPSuM, S4: S40RTS, S3: S362ANI, US: US.2016, SE: SEMum-NA14, KR: Krischer18. Models UL, S4, S3 and SE are implemented with Crust1.0 on top.

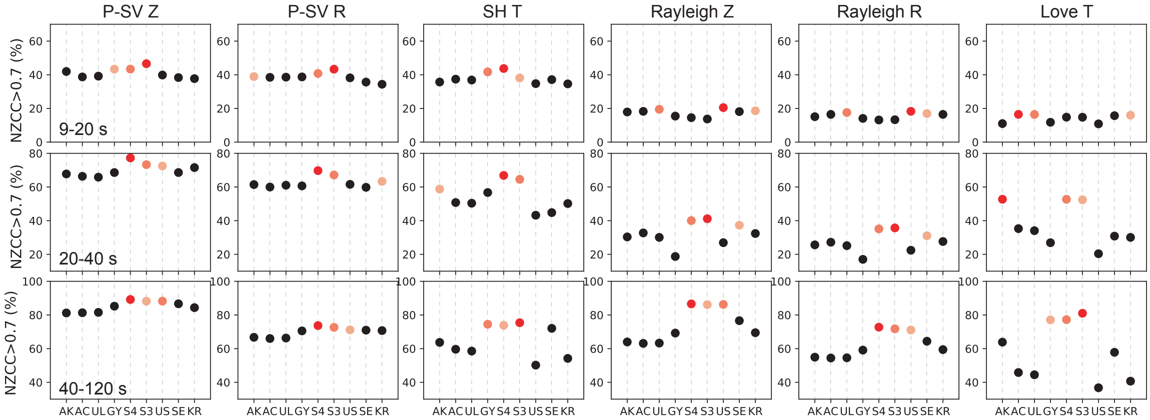

Figure 10. Model predictability defined by the percentage of NZCC>0.7. Rows upper to lower: 9-20 s, 20-40 s and 40-120 s; Panels left to right: 6 categories (P-SV Z, P-SV R, SH T, Rayleigh Z, Rayleigh R and Love T). First 3 models with maximum percentage of NZCC>0.7 measurements are marked with different reds. The x-axis marks are for different models: AK: AK135, AC: AK135+Crust1.0, UL: US-SL-2014, GY: GyPSuM, S4: S40RTS, S3: S362ANI, US: US.2016, SE: SEMum-NA14, KR: Krischer18. Models UL, S4, S3 and SE are implemented with Crust1.0 on top.

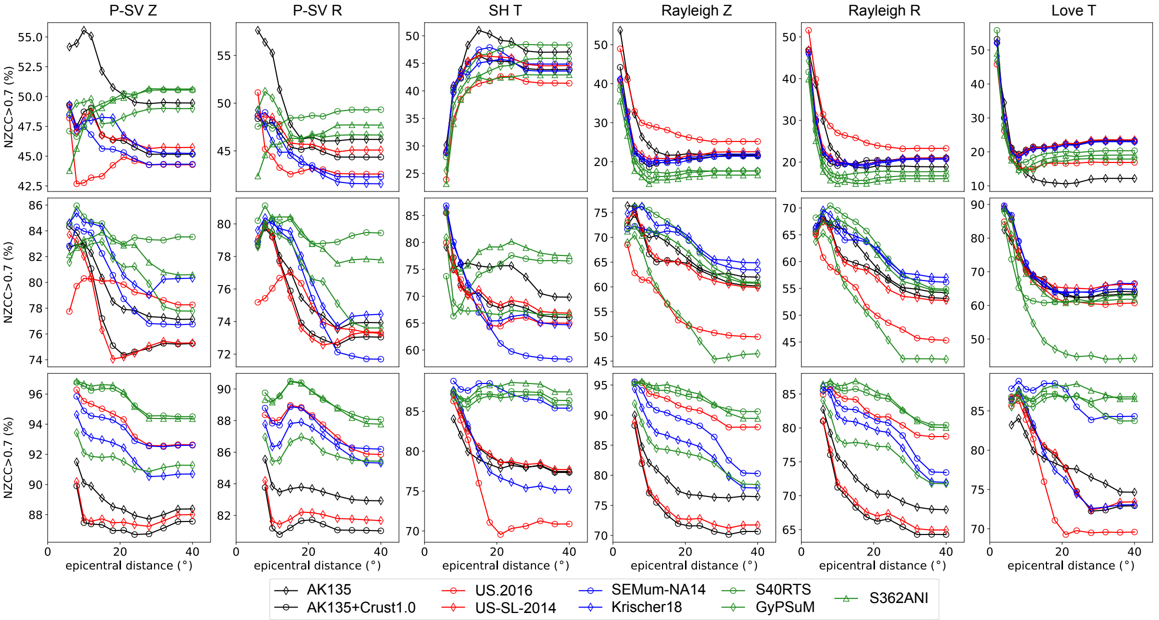

Figure 11. Model predictability vs. different epicentral distances. The percentage of measurements with NZCC>0.7 within certain epicentral distances are plotted for different seismic phases in 6 categories (columns left to right: P-SV Z, P-SV R, SH T, Rayleigh Z, Rayleigh R and Love T) in different period ranges (rows top to bottom, 9–20 s, 20–40 s, and 40–120 s). Higher percentages indicate better model predictability.

REFERENCES

Alex Song, T.-R. & Helmberger, D. V., 2007. Validating tomographic model with broad-band waveform modelling: an example from the la ristra transect in the southwestern united states, *Geophysical Journal International*, **171**(1), 244–258.

Bedle, H. & van der Lee, S., 2009. S velocity variations beneath north america, *Journal of Geophysical Research: Solid Earth*, **114**(B7).

Bozdağ, E. & Trampert, J., 2010. Assessment of tomographic mantle models using spectral element seismograms, *Geophysical Journal International*, **180**(3), 1187–1199.

Buehler, J. & Shearer, P., 2017. Uppermost mantle seismic velocity structure beneath usarray, *Journal of Geophysical Research: Solid Earth*, **122**(1), 436–448.

Burdick, S., Vernon, F. L., Martynov, V., Eakins, J., Cox, T., Tytell, J., Mulder, T., White, M. C., Astiz, L., Pavlis, G. L., et al., 2017. Model update may 2016: Upper-mantle heterogeneity beneath north america from travel-time tomography with global and usarray data, *Seismological Research Letters*, **88**(2A), 319–325.

Chen, M., Niu, F., Liu, Q., & Tromp, J., 2015a. Mantle-driven uplift of hangai dome: New seismic constraints from adjoint tomography, *Geophysical Research Letters*, **42**(17), 6967–6974.

Chen, M., Niu, F., Liu, Q., Tromp, J., & Zheng, X., 2015b. Multiparameter adjoint tomography of the crust and upper mantle beneath east asia: 1. model construction and comparisons, *Journal of Geophysical Research: Solid Earth*, **120**(3), 1762–1786.

Chen, M., Niu, F., Tromp, J., Lenardic, A., Lee, C.-T. A., Cao, W., & Ribeiro, J., 2017. Lithospheric foundering and underthrusting imaged beneath tibet, *Nature communications*, **8**, 15659.

Chen, M., Manea, V. C., Niu, F., Wei, S. S., & Kiser, E., 2019. Genesis of intermediate-depth and deep intraslab earthquakes beneath japan constrained by seismic tomography, seismicity, and thermal modeling, *Geophysical Research Letters*, **46**(4), 2025–2036.

Coffin, M. F., Eldholm, O., et al., 2005. Large igneous provinces, *Encyclopedia of Geology*, pp. 315–323.

Coleman Jr, J. L. & Cahan, S. M., 2012. Preliminary catalog of the sedimentary basins of the united states.

Ekström, G., Nettles, M., & Dziewoński, A., 2012. The global cmt project 2004–2010: Centroid-moment tensors for 13,017 earthquakes, *Physics of the Earth and Planetary Interiors*, **200**, 1–9.

Engdahl, E. R., van der Hilst, R., & Buland, R., 1998. Global teleseismic earthquake relocation with improved travel times and procedures for depth determination, *Bulletin of the Seismological Society of America*, **88**(3), 722–743.

Fichtner, A., Kennett, B. L., Igel, H., & Bunge, H.-P., 2009. Full seismic waveform tomography for upper-mantle structure in the australasian region using adjoint methods, *Geophysical Journal International*, **179**(3), 1703–1725.

Fichtner, A., Kennett, B. L., Igel, H., & Bunge, H.-P., 2010. Full waveform tomography for radially anisotropic structure: new insights into present and past states of the australasian upper mantle, *Earth and Planetary Science Letters*, **290**(3-4), 270–280.

Gao, H. & Shen, Y., 2012. Validation of shear-wave velocity models of the pacific northwest, *Bulletin of the Seismological Society of America*, **102**(6), 2611–2621.

Gao, H. & Shen, Y., 2015. Validation of recent shear wave velocity models in the united states with full-wave simulation, *Journal of Geophysical Research: Solid Earth*, **120**(1), 344–358.

Jiang, C., Schmandt, B., Hansen, S. M., Dougherty, S. L., Clayton, R. W., Farrell, J., & Lin, F.-C., 2018. Rayleigh and s wave tomography constraints on subduction termination and lithospheric foundering in central california, *Earth and Planetary Science Letters*, **488**, 14–26.

Kennett, B. L., Engdahl, E., & Buland, R., 1995. Constraints on seismic velocities in the earth from traveltimes, *Geophysical Journal International*, **122**(1), 108–124.

Komatitsch, D. & Tromp, J., 2002a. Spectral-element simulations of global seismic wave propagation—i. validation, *Geophysical Journal International*, **149**(2), 390–412.

Komatitsch, D. & Tromp, J., 2002b. Spectral-element simulations of global seismic wave propagation—ii. three-dimensional models, oceans, rotation and self-gravitation, *Geophysical Journal International*, **150**(1), 303–318.

Krischer, L., Fichtner, A., Boehm, C., & Igel, H., 2018. Automated large-scale full seismic waveform inversion for north america and the north atlantic, *Journal of Geophysical Research: Solid Earth*, **123**(7), 5902–5928.

Kustowski, B., Ekström, G., & Dziewoński, A., 2008. Anisotropic shear-wave velocity structure of the earth's mantle: A global model, *Journal of Geophysical Research: Solid Earth*, **113**(B6).

Laske, G., Masters, G., Ma, Z., & Pasyanos, M., 2013. Update on crust1. 0—a 1-degree global model of earth's crust, in *Geophys. Res. Abstr*, vol. 15, p. 2658, EGU General Assembly Vienna, Austria.

Lekić, V. & Romanowicz, B., 2011. Inferring upper-mantle structure by full waveform tomography with the spectral element method, *Geophysical Journal International*, **185**(2), 799–831.

Lin, F.-C., Schmandt, B., & Tsai, V. C., 2012. Joint inversion of rayleigh wave phase velocity and ellipticity using usarray: Constraining velocity and density structure in the upper crust, *Geophysical Research Letters*, **39**(12).

Lin, F.-C., Tsai, V. C., & Schmandt, B., 2014. 3-d crustal structure of the western united states: application of rayleigh-wave ellipticity extracted from noise cross-correlations, *Geophysical Journal International*, **198**(2), 656–670.

Liu, Y., Teng, J., Xu, T., Wang, Y., Liu, Q., & Badal, J., 2016. Robust time-domain full waveform inversion with normalized zero-lag cross-correlation objective function, *Geophysical Journal International*, **209**(1), 106–122.

Montelli, R., Nolet, G., Masters, G., Dahlen, F., & Hung, S.-H., 2004. Global p and pp traveltime tomography: rays versus waves, *Geophysical Journal International*, **158**(2), 637–654.

Mulder, W. & Plessix, R.-E., 2008. Exploring some issues in acoustic full waveform inversion, *Geo-*

physical Prospecting, **56**(6), 827–841.

Nelson, P. L. & Grand, S. P., 2018. Lower-mantle plume beneath the yellowstone hotspot revealed by core waves, *Nature Geoscience*, **11**(4), 280.

Pavlis, G. L., Sigloch, K., Burdick, S., Fouch, M. J., & Vernon, F. L., 2012. Unraveling the geometry of the farallon plate: Synthesis of three-dimensional imaging results from usarray, *Tectonophysics*, **532**, 82–102.

Porritt, R. W., Allen, R. M., & Pollitz, F. F., 2014. Seismic imaging east of the rocky mountains with usarray, *Earth and Planetary Science Letters*, **402**, 16–25.

Qin, Y., Capdeville, Y., Montagner, J.-P., Boschi, L., & Becker, T. W., 2009. Reliability of mantle tomography models assessed by spectral element simulation, *Geophysical Journal International*, **177**(1), 125–144.

Ritsema, J., Van Heijst, H., Woodhouse, J., & Deuss, A., 2009. Long-period body wave traveltimes through the crust: implication for crustal corrections and seismic tomography, *Geophysical Journal International*, **179**(2), 1255–1261.

Ritsema, J., Deuss, a. A., Van Heijst, H., & Woodhouse, J., 2011. S40rts: a degree-40 shear-velocity model for the mantle from new rayleigh wave dispersion, teleseismic traveltime and normal-mode splitting function measurements, *Geophysical Journal International*, **184**(3), 1223–1236.

Robertsson, J. O., 1996. A numerical free-surface condition for elastic/viscoelastic finite-difference modeling in the presence of topography, *Geophysics*, **61**(6), 1921–1934.

Ruan, Y., Lei, W., Modrak, R., Örsvuran, R., Bozdağ, E., & Tromp, J., 2019. Balancing unevenly distributed data in seismic tomography: a global adjoint tomography example, *Geophysical Journal International*, **219**(2), 1225–1236.

Schmandt, B. & Humphreys, E., 2010. Complex subduction and small-scale convection revealed by body-wave tomography of the western united states upper mantle, *Earth and Planetary Science Letters*, **297**(3-4), 435–445.

Schmandt, B. & Lin, F.-C., 2014. P and s wave tomography of the mantle beneath the united states, *Geophysical Research Letters*, **41**(18), 6342–6349.

Schmandt, B., Lin, F.-C., & Karlstrom, K. E., 2015. Distinct crustal isostasy trends east and west of the rocky mountain front, *Geophysical Research Letters*, **42**(23), 10–290.

Shen, W. & Ritzwoller, M. H., 2016. Crustal and uppermost mantle structure beneath the united states, *Journal of Geophysical Research: Solid Earth*, **121**(6), 4306–4342.

Simmons, N. A., Forte, A. M., Boschi, L., & Grand, S. P., 2010. Gypsum: A joint tomographic model of mantle density and seismic wave speeds, *Journal of Geophysical Research: Solid Earth*, **115**(B12).

Tao, K., Grand, S. P., & Niu, F., 2017. Full-waveform inversion of triplicated data using a normalized-correlation-coefficient-based misfit function, *Geophysical Journal International*, **210**(3), 1517–1524.

Tao, K., Grand, S. P., & Niu, F., 2018. Seismic structure of the upper mantle beneath eastern asia from full waveform seismic tomography, *Geochemistry, Geophysics, Geosystems*, **19**(8), 2732–2763.

Tape, C., Liu, Q., Maggi, A., & Tromp, J., 2009. Adjoint tomography of the southern california crust, *Science*, **325**(5943), 988–992.

Tape, C., Liu, Q., Maggi, A., & Tromp, J., 2010. Seismic tomography of the southern california crust based on spectral-element and adjoint methods, *Geophysical Journal International*, **180**(1), 433–462.

Tromp, J., Tape, C., & Liu, Q., 2005. Seismic tomography, adjoint methods, time reversal and banana-doughnut kernels, *Geophysical Journal International*, **160**(1), 195–216.

van der Kruk, J., Gueting, N., Klotzsche, A., He, G., Rudolph, S., von Hebel, C., Yang, X., WeihermŘller, L., Mester, A., & Vereecken, H., 2015. Quantitative multi-layer electromagnetic induction inversion and full-waveform inversion of crosshole ground penetrating radar data, *Journal of Earth Science*, **26**(6), 844–850.

Yuan, H., French, S., Cupillard, P., & Romanowicz, B., 2014. Lithospheric expression of geological units in central and eastern north america from full waveform tomography, *Earth and Planetary Science Letters*, **402**, 176–186.

Zhou, T., Meng, L., Xie, Y., & Han, J., 2019. An adjoint-state full-waveform tsunami source inversion method and its application to the 2014 chile-iquique tsunami event, *Journal of Geophysical Research: Solid Earth*, **124**(7), 6737–6750.

Zhu, H., Komatitsch, D., & Tromp, J., 2017. Radial anisotropy of the north american upper mantle based on adjoint tomography with usarray, *Geophysical Journal International*, **211**(1), 349–377.

Supplementary information

1 More waveform comparison on 40-120 s

For long period (40-120 s) body and surface waves, the waveform fitting for all the models are generally improving. Models S40RTS and S362ANI are among the best. We need to notice that at such a long period, the shear wave and surface wave are merged together at shorter epicentral distances. In Fig. A1, the waveform in traces with epicentral distance below 25 degrees will have surface wave components. Similarly, traces with epicentral distance below 25 degrees will have a portion of shear waves component.

Figure A1. Waveform comparison for long period shear wave. The seismic recordings are filtered between 40–120 s and aligned with the theoretical arrival time of S-wave. Black and red lines are the observed and synthetic waveforms, respectively. Blue dashed lines mark the shear wave measurement window. Cyan dashed line indicates the starting of surface wave calculated by empirical surface wave speeds in Table. 2. Models S40RTS, S362ANI, US-SL-2014, and SEMum-NA14 have Crust1.0 on top.

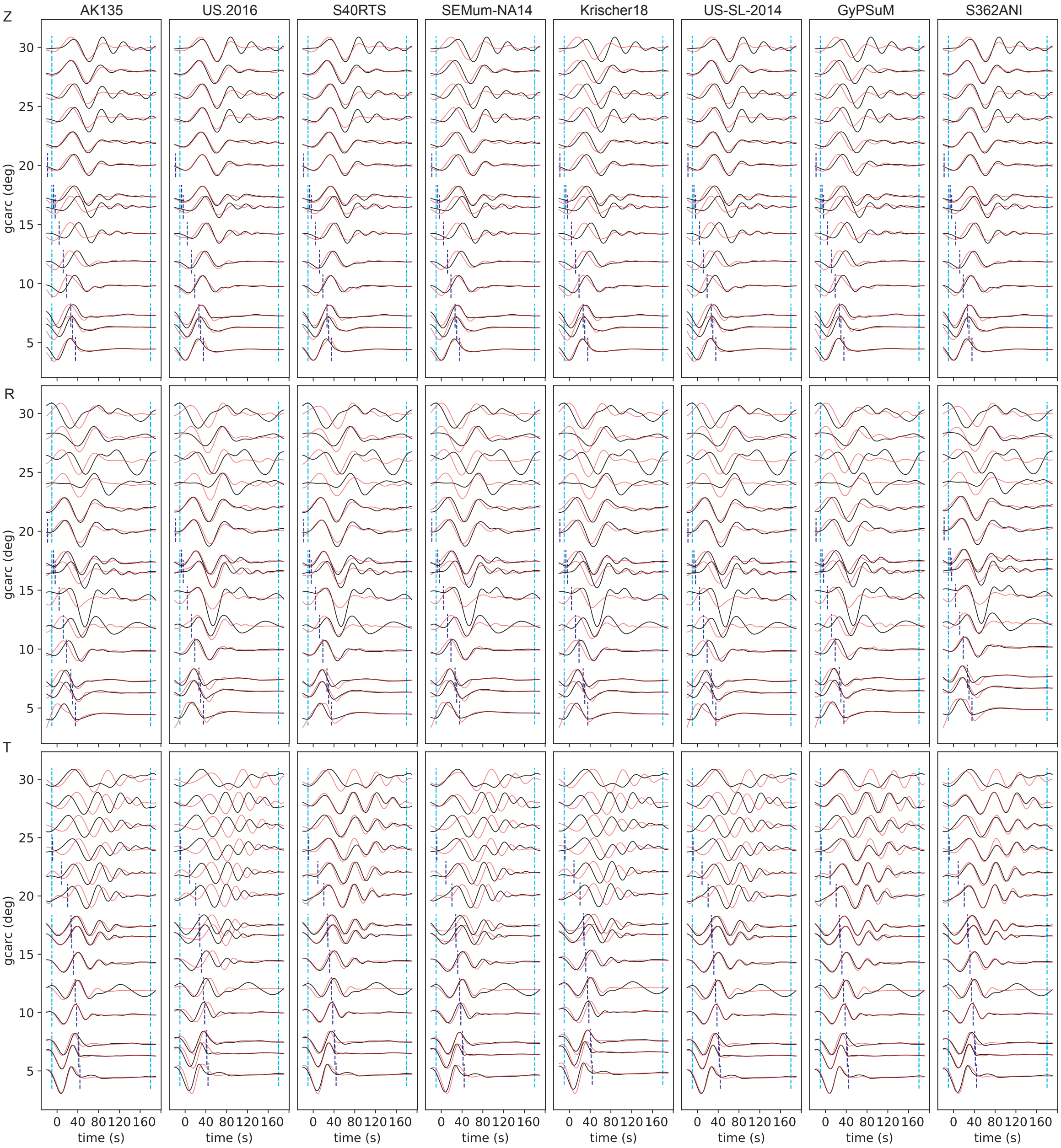

Figure A2. Waveform comparison for long period surface wave. The seismic recordings are filtered between 40–120 s and aligned with the empirical arrival time of Rayleigh or Love waves. Black and red lines are the observed and synthetic waveforms, respectively. Cyan dashed lines mark the surface wave measurement window. Blue dashed line indicates the end of shear wave calculated by 60 seconds after empirical S wave arrival time calculated by 1-D model AK135.

2 Basin structure along the measuring line

The complicated shear wave recorded by the long-epicentral distance stations especially in short period ranges (Figure 3-6) is most likely to be related to shallow structures. The coda waves in 9-20 s looks like the basin reverberations. We plot the averaged shear wave velocity within the 20 degrees aperture along the E-W profile of earthquake 201305240347A in the figure below. The stations in around 82-85 degrees east are related to a local sedimentary basin.

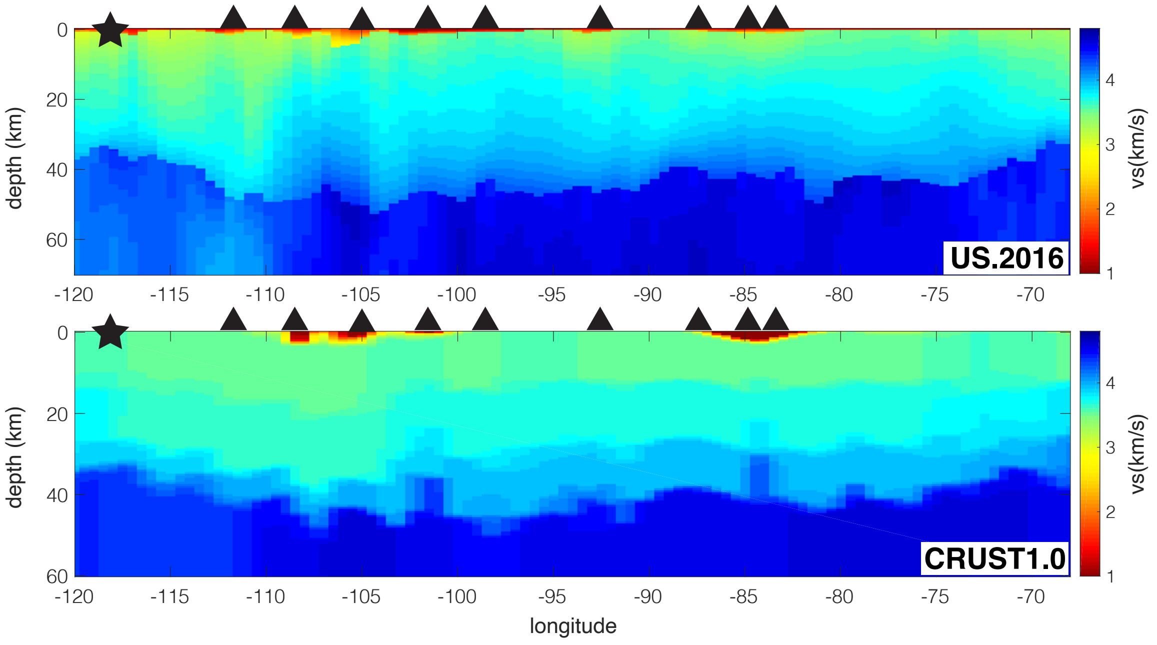

Figure A3. Cross section of the averaged shear wave velocity along 40°E within a 20° aperture angle of models US.2016 and CRUST1.0. Star is showing the earthquake 201305240347A and triangles are showing the projection of the stations in Fig. 3.

3 Travel time error distribution histogram by separating surface wave and body wave

In the body wave travel time shift distribution histogram, it seems that for short period range (9-20 s) and long period range (40-120 s), every model has similar standard deviation. In 20-40 s intermediate period range, models S40RTS and S362ANI has significant lower standard deviation than other models. There is still systematic negative mean for almost every model in every period ranges. For the surface wave travel time shift distribution, models AK135 and AK135+Crust1.0 have significant higher standard deviation than other models in 9-20 s period range, while in intermediate and long period range, models S40RTS and S362ANI has significantly lower standard deviation. The systematic negative error still presents, except for model GyPSuM. The radial anisotropy feature of the contiguous U.S and surrounding regions are captured by models SEMum-NA14, Krischer18 and S362ANI. The travel time distribution of both SV and SH are more centralized with similar shape, while other models have a slightly systematically slower mean SH wave travel time. For the Love wave, we observe similar phenomena compared to Rayleigh wave (Figs. A4 and A6).

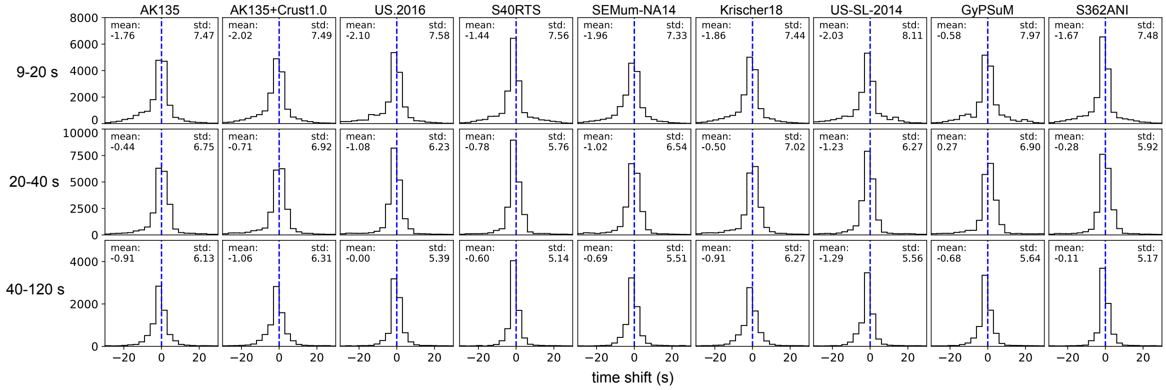

Figure A4. Travel time shift distribution histograms for body wave only measurement windows. Rows upper to lower: 9-20 s, 20-40 s and 40-120 s; Panels left to right: different models.

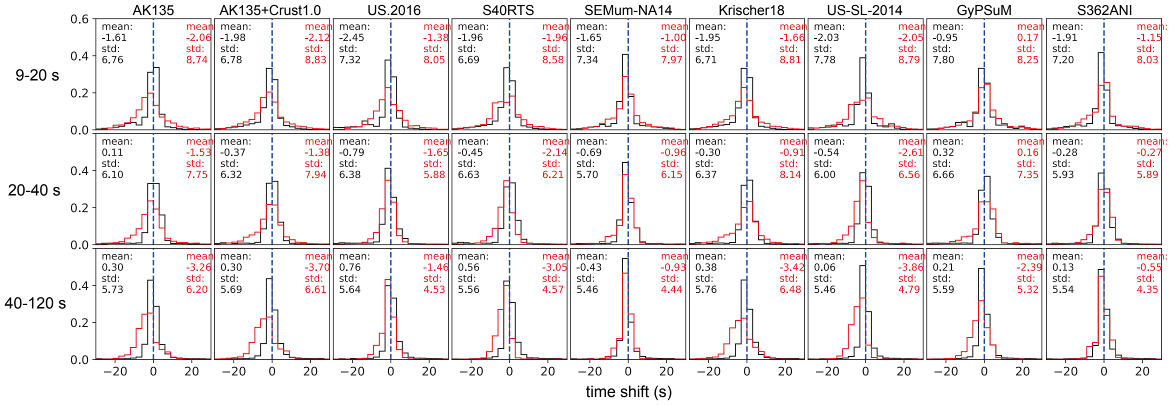

Figure A5. Travel time shift distribution histograms for SV and SH waves. Black and red lines and texts are for SV and SH, respectively. Rows upper to lower: 9-20 s, 20-40 s and 40-120 s; Panels left to right: different models.

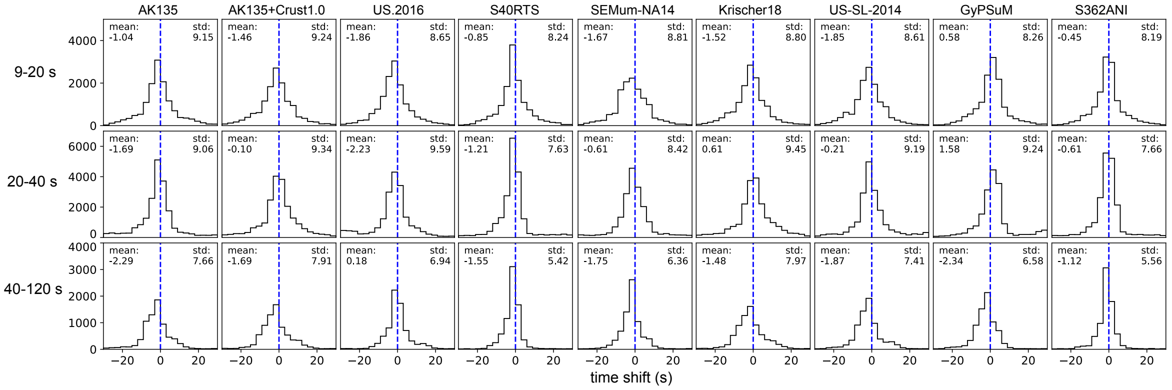

Figure A6. Travel time shift distribution histograms for surface wave only measurement windows. Rows upper to lower: 9-20 s, 20-40 s and 40-120 s; Panels left to right: different models.

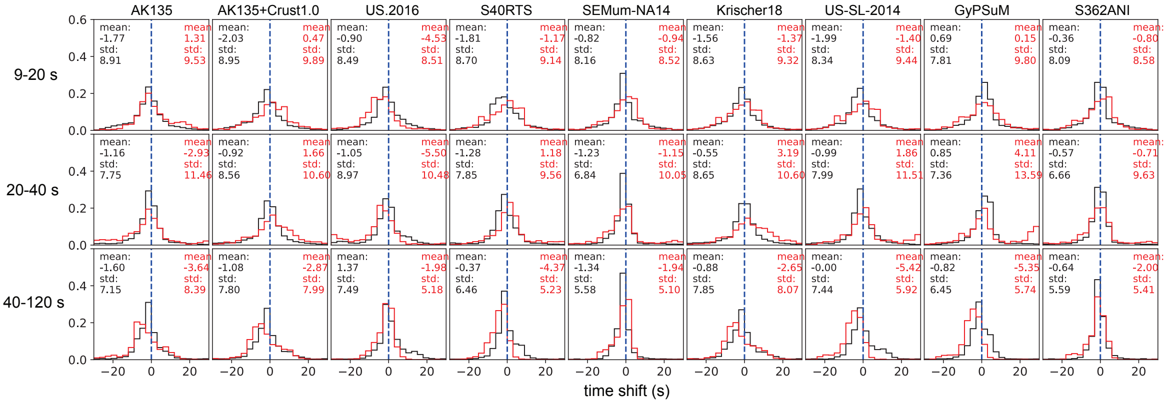

Figure A7. Travel time shift distribution histograms for Rayleigh and Love waves. Black and red lines and texts are for Rayleigh and Love, respectively. Rows upper to lower: 9-20 s, 20-40 s and 40-120 s; Panels left to right: different models.

4 Travel time, amplitude, waveform and NZCC misfit figures by separating surface wave and body wave

The body wave misfits are basically similar to the overall misfits, while the surface wave misfits are overall larger, indicating the surface waves, especially in short periods, are not well fitted by current models.

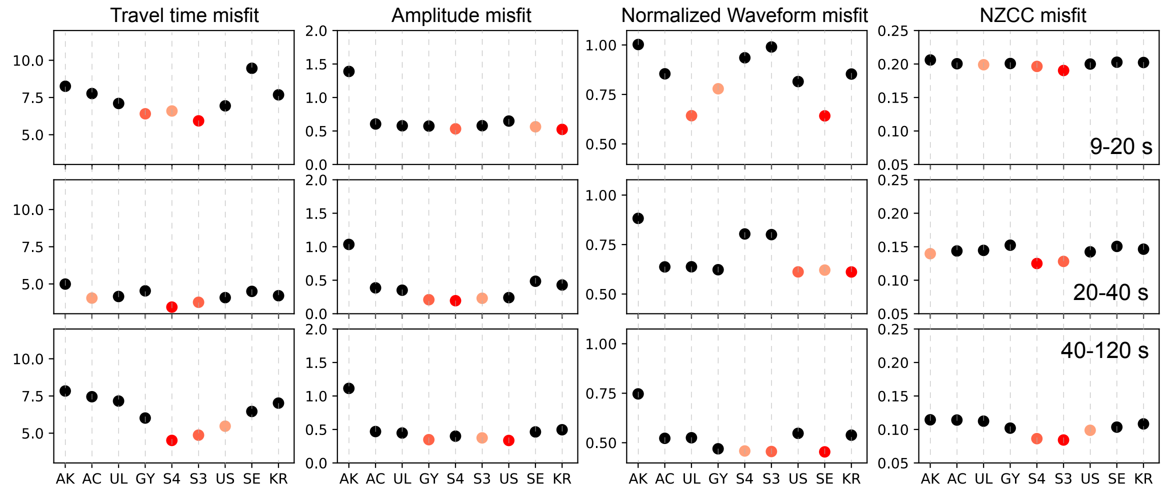

Figure A8. Travel time shift distribution histograms for body wave only measurement windows. Rows upper to lower: 9-20 s, 20-40 s and 40-120 s; Panels left to right: different models.

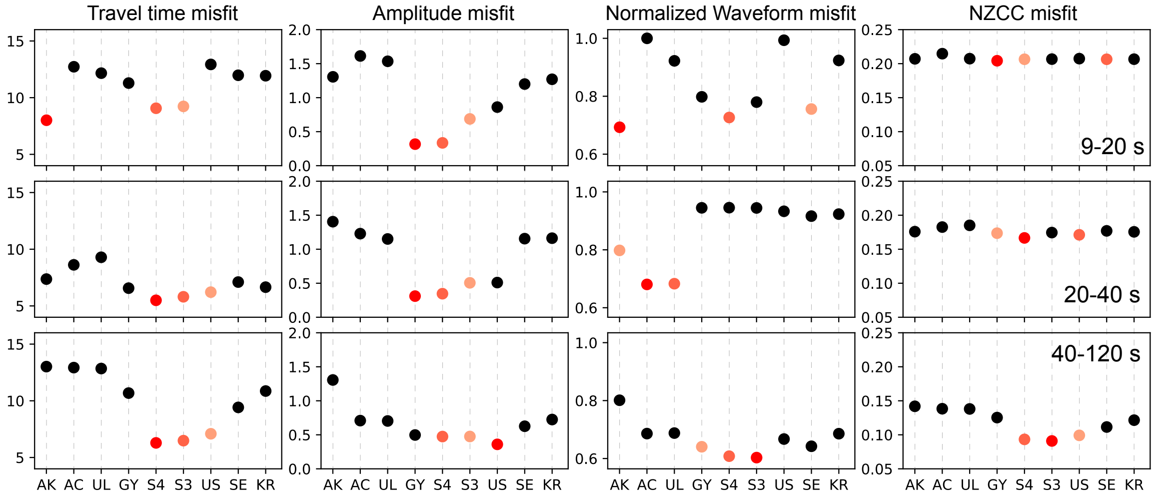

Figure A9. Travel time shift distribution histograms for surface wave only measurement windows. Rows upper to lower: 9-20 s, 20-40 s and 40-120 s; Panels left to right: different models.